Liquid Foams of Graphene

by

Daniel Alcazar Jorba

M.S. Materials Science and Engineering
Massachusetts Institute of Technology (2008)

Submitted to the Department of Materials Science and Engineering
in Partial Fulfillment of the Requirements for the Degree of
Doctor of Philosophy in Materials Science and Engineering
at the
Massachusetts Institute of Technology
June 2012

Signature of Author ……..
Department of Materials Science and Engineering
May 14, 2012

Certified by…….....
Edwin L. Thomas
Professor of Materials Science and Engineering
Thesis Supervisor

Accepted by.....
Gerbrand Ceder
R. P. Simmons Professor of Materials Science and Engineering
Chair, Departmental Committee on Graduate Students

Liquid Foams of Graphene

by

Daniel Alcazar Jorba

Submitted to the Department of Materials Science and Engineering on May 24, 2012

in Partial Fulfillment of the Requirements for the Degree of

Doctor of Philosophy in Materials Science and Engineering

Abstract

Liquid foams are dispersions of bubbles in a liquid. Bubbles are stabilized by foaming agents that position at the interface between the gas and the liquid. Most foaming agents, such as the commonly used sodium dodecylsulfate, are surfactant molecules with linear or branched chain molecular structures. This thesis presents a new class of liquid foams made with a foaming agent having a sheet molecular structure. In these foams, air bubbles are encapsulated inside graphene shells. The shells have a concentric layered structure made of isophorone diamine modified graphene oxide sheets.

The liquid foams of graphene were initially developed as an extractive step in the preparation of graphene-epoxy nanocomposites. Chapter 1 gives an introduction to polymer nanocomposites and graphene. Chapter 2 presents a novel processing method for graphene-epoxy nanocomposites. Chapter 3 deals with the structure, formation mechanism, stability and mechanical properties of the liquid foams of graphene. Chapter 4 reports on materials and methods. Finally, Chapter 5 summarizes the main conclusions of this work and proposes future directions for research.

Thesis supervisor: Edwin L. Thomas

Title: Professor of Materials Science and Engineering

Acknowledgements

I would like gratefully to acknowledge the help and support I have received from my thesis supervisor, Prof. Edwin L. Thomas, and thesis committee members, Prof. Lorna J. Gibson and Prof. Timothy M. Swager, as well as from faculty, staff and peers at the Department of Materials Science and Engineering, the Department of Chemistry, the Institute for Soldier Nanotechnologies and the Center for Materials Science and Engineering. I would like to thank Prof. Bernard Lotz for encouraging and supporting me to come to graduate school at MIT. I would also like to thank Prof. Georges Hadziioannou and Dr. Annette Thierry for their support.

Contents

Chapter 1. Introduction

1.1. Carbon blacks

1.2. Polymer nanocomposites

1.2.1. Nanoclays

1.2.2. Carbon nanotubes

1.3. Graphene

Chapter 2. Processing method for graphene-epoxy nanocomposites

2.1. Introduction

2.2. Processing method

2.2.1. Preparation of graphene oxide

2.2.2. Modification of graphene oxide with isophorone diamine

2.2.3. Formation of the liquid foam of graphene

2.2.4. Mixing of the foam with isophorone diamine and dehydration

2.2.5. Compounding and curing

2.3. Analysis of the graphene sheets along the processing stages

2.3.1. Overview

2.3.2. X-ray photoelectron spectroscopy

2.3.3. X-ray diffraction

2.3.4. Transmission electron microscopy

Chapter 3. Liquid foams of graphene

3.1. Introduction

3.2. Structure of the foams

3.3. Graphene foaming mechanism

3.4. Mechanical properties of the graphene shells

Chapter 4. Materials and methods

Chapter 5. Conclusions and future directions

References

Chapter 1

Introduction

This chapter gives a background on carbon black composites, polymer nanocomposites and graphene. The section on polymer nanocomposites contains parts dedicated to nanoclays and carbon nanotubes (CNTs).

1.1. Carbon blacks

Carbon blacks are used as pigments, for ultraviolet protection and to enhance electrical and mechanical properties of polymers. They are primarily used as reinforcing agent for elastomers. Carbon blacks are spheroidal particles from 10 nm to 50 nm in diameter clustered together in aciniform aggregates. The diameter of the equivalent sphere of the aggregates ranges from 100 nm to 500 nm.

Most carbon blacks are produced from oil by the furnace process. The composition of furnace blacks contains from 0.5 % to 2 % of oxygen (O) atoms and from 1 % to 2 % of sulfur (S) atoms. Different grades are distinguished by their specific surface area, aggregate morphology, and surface chemistry.[1] The density of carbon black particles ranges from 2.04 g/cm^3 to 2.11 g/cm^3 according to x-ray diffraction (XRD) measurements of interlayer spacing.[2]

The presence of S atoms on the surface of carbon blacks improves the mechanical properties of vulcanized rubbers. Upon curing, S moieties form covalent bonds with the elastomeric matrix, for example in the manufacture of tires. Heating carbon black to 2700 °C eliminates most of the surface functional groups reducing the ability to form bonds with the matrix which limits its reinforcing action.[3]

The electrical conductivity of carbon blacks ranges from 10 S/m to 10^4 S/m. The typical conductivity of percolating carbon black networks in polymer matrices is around 1

S/m. The electrical percolation threshold depends on the type of resin system, carbon black grade and processing method. Percolation thresholds range from 1 wt % to 4 wt % for conductive grades and from 5 wt % to 40 wt % for general grades. Surface functional groups and impurities are known to decrease the electrical conductivity of carbon blacks. Surface functional groups also affect the interaction with liquid or molten resins which affects the dispersion of carbon black in the polymer matrix. The influence of processing on electrical conductivity presents an optimum mixing time where aggregate breakdown balances with improved dispersion.[4] Higher aggregation and broader distribution of particle and aggregate size facilitates electrical percolation.[5] However, those characteristics contributing to higher electrical conductivity, namely high aggregation, high surface area and low degree of surface functionalization also cause higher resin viscosity.[6]

In a study on the mechanical properties of carbon black filled epoxy resins, Gojny et al. showed that adding 0.5 wt % of carbon black to epoxy resins resulted in a moderate increase in stiffness and tensile strength and enhanced fracture toughness compared to the neat epoxy. The elastic modulus improved by 9 % from 2.59 GPa to 2.83 GPa, the ultimate tensile strength increased by 2 % from 63.8 MPa to 65.34 MPa and the mode I fracture toughness increased by 30 % from 0.65 $MPa.m^{½}$ to 0.85 $MPa.m^{½}$.[7]

1.2. Polymer nanocomposites

The polymer market is experiencing a rapid growth of a new type of formulations known as nanocomposites. Nanocomposites are mixtures of polymer resins and nanoscale high aspect-ratio additives. The high aspect-ratio of the additives is what differentiates nanocomposites from traditional polymer composites.

Carbon blacks have nanometer scale dimensions but their spheroidal morphology results in aspect-ratios of 1. In contrast, nanoscale additives with rod and sheet morphologies like CNTs and nanoclays can attain aspect-ratios of 10,000 and 1,000 respectively.[8]

Additives with high aspect-ratios can enhance the properties of polymers at low loadings. Properties like electrical conductivity experience a sharp change upon reaching a critical volume fraction of additive. At this critical additive loading, conductive additive particles are able to create a percolation pathway through the matrix. The critical volume fraction of additive for percolation (f_c) is known as the percolation threshold where f is the volume fraction of the additive particles in the matrix. At the electrical percolation threshold, additive particles are able to form a connecting cluster that will allow electron transport through the otherwise insulating polymer matrix. The value of f_c depends on the shape of the additive particle. Spherical additives present a $f_c \sim 0.16$ whereas additives with rod shapes have $f_c < 0.16$. The percolation threshold is inversely proportional to the aspect-ratio of the additive particles. Provided the additive particles are homogeneously dispersed in the polymer matrix, rod-like particles form connective pathway at lower loadings compared to spherical

particles and rod-like particles of increasing aspect-ratios will form connective pathways easily.[9]

Low additive loading avoids detrimental side effects such as brittleness, increased viscosity, and rougher surface finish and may be a potential source of cost reduction. The following is an overview on nanoclays and CNTs. Nanoclays and CNTs are the two main additives commercially used in nanocomposites.

1.2.1. Nanoclays

Nanoclays can improve the mechanical, thermal and barrier properties as well as enhance flame retardancy of polymers. They are commercially used as reinforcing agents for polyamides and polyolefins in automobile components and as gas barrier additives for polyamides in food packaging.

Nanoclays are obtained from layered silicates. In silicates belonging to the family of phyllosilicates, layers are made of sheets having a thickness around 1 nm. The lateral dimensions of the sheets vary from tens of nanometers to several microns resulting in aspect-ratios up to 1,000.[10]

The space between sheets in silicates is occupied by hydrated alkali metal cations. The dispersion of nanoclays in polymers involves the exfoliation of the sheets from the layered

silicates. This can be done via two routes, transforming the hydrophilic silicates into organophilic forms followed by intercalation of organophilic polymer or pre-polymer resins or direct intercalation of hydrophilic polymers in the hydrophilic silicates.

Usuki et al. employed ion exchange reactions with cationic surfactants such as alkylammonium cations to convert the hydrophilic surface of the sheets into an organophilic surface. These organophilic silicates are called organosilicates and present better compatibility with hydrophobic polymers.[11]

XRD analysis of interlayer spacing in silicates enables to monitor the intercalation of polymers and pre-polymers in between the sheets. Messersmith and Giannelis studied the intercalation of epoxy resins in an organically modified mica-type Na-montmorillonite silicate. XRD measurements using in-situ hot-stage enabled tracking the evolution of the interlayer spacing during intercalation of the epoxy precursor. At room temperature, the organosilicate powder showed a main reflection at $2\theta = 4.8°$ corresponding to the layer spacing of 1.7 nm (d_{001}). This was already a 0.7 nm increase with respect to the interlayer spacing in the hydrophilic un-modified Na-montmorillonite. Upon mixing with the epoxy precursor at room temperature, a new reflection at $2\theta = 2.5°$ emerged which was assigned to the layer spacing in the intercalated organosilicate-epoxy (d_{001} = 3.5 nm). Upon heating at 90 °C for 1 hour, only reflections corresponding to the epoxy intercalated organosilicate were observed corresponding to the first, second and third-order reflections of the interlayer spacing, at $2\theta = 2.5°$, 4.9° and 7.6° respectively.[12]

Vaia et al. accomplished the direct intercalation of poly(ethylene oxide) in an hydrophilic silicate upon heating the mixture of polymer and silicate at 80°C. After six hours, the XRD pattern showed reflections corresponding to the poly(ethylene oxide) intercalated silicate only.[13]

Kato and Usuki reviewed the properties of organosilicate filled polyamide nanocomposites. At a loading of 4.2 wt %, they reported an increase of tensile modulus from 1.1 GPa to 2.1 GPa, an increase in tensile strength from 69 MPa to 107 MPa and an improvement in impact strength from 2.3 KJ/m^2 to 2.8 KJ/m^2. The heat distortion temperature increased from 65 °C up to 152 °C. The thermal analysis showed an increase in glass transition temperature from 65 °C to 150 °C.[14]

Polymer matrices experience an improvement in barrier properties upon addition of nanoclays. Nanoclays filled polymers show enhanced impermeability to liquids and gases. The concept of tortuous path is used to explain the lower diffusivity through a matrix containing a homogeneous dispersion of sheets. Messersmith and Giannelis studied the permeability to moisture of poly(epsilon-caprolactone) filled with an organically modified mica-type silicate. The water vapor permeability of films showed a linear dependence on nanoclay content. At a 4.8 vol. % loading (9.5 wt %, assuming a density for poly(epsilon-caprolactone) of 1.2 g/cm^3 and a density for mica-type silicate of 2.5 g/cm^3), the water vapor permeability decreased by 80 % compared to the neat polymer.[15]

1.2.2. Carbon nanotubes

CNTs can improve the mechanical and electrical properties as well as enhance flame retardancy of polymers. CNTs can be single-wall (SWCNTs) or multi-wall (MWCNTs), the later consisting in nested arrangements of SWCNTs. SWCNTs have a diameter from around 1 to 2 nm while the diameter of MWCNTs can be as high as several hundred nanometers. With typical lengths of tens of microns, CNTs can present aspect-ratios of 10,000.[16]

CNTs are produced via the following three processes: arc discharge, laser ablation and chemical vapor deposition. Current production technologies yield CNTs with a distribution of structures, diameters and lengths. CNTs can be produced in the form of bundles, vertically aligned on substrates and pulled into fibers.[17] The majority of industrial methods produce CNTs in the form of bundles. De-bundling is then required to attain homogeneous dispersions of CNTs in polymer matrices. However, most often nanotubes can only be processed in the form of dispersions of small bundles. Several methods for processing CNT-polymer nanocomposites are reviewed below.

The mechanical and electrical properties of individual CNTs have been investigated from both theoretical and experimental standpoints. Theoretical calculations predict values for the elastic modulus of SWCNTs around 1 TPa.[18] Yu et al. carried out experimental measurements of the stress-strain response on individual MWCNTs and found tensile strength values ranging from 11 to 63 GPa and values for the Young's modulus ranging from 270 to 950 GPa. They observed that MWCNTs failed after the outermost layer broke.[19] In another

study, Yu et al. found that bundles of SWCNT have breaking strengths ranging from 13 GPa to 52 GPa and a Young's moduli between 320 GPa and 1,470 GPa.[20]

The molecular structure of CNTs determines if they are metals or semiconductors. The electrical conductivity of individual CNTs can be 10^8 S/m for metallic SWCNTs,[21] and $3x10^6$ S/m for MWCNTs.[22] Bundles of CNTs present values of electrical conductivity of $1.5x10^4$ S/m.[23]

The quality of the dispersion of CNTs in the polymer matrix is critical to nanocomposite performance. Solution mixing, melt mixing, in-situ polymerization, and the use of surfactants are the most common approaches to disperse CNTs in polymer matrices.

The use of surfactants can facilitate de-bundling by reducing van der Waals interactions between CNTs in addition to stabilize the interface with the polymer matrix. Following this approach, Gong et al. dispersed 1 wt % CNT in an epoxy resin with the aid of 1 wt % polyoxyethylene 8 lauryl resulting in a 30 % increase in Young's modulus. An increase in glass transition temperature was also reported from 63 °C for the neat epoxy to 88 °C for the mixture.[24]

An alternative to using surfactants is to covalently functionalize the surface of CNTs.[25] Gojny et al. conducted a comparative study of the reinforcing effect of functionalized vs. un-functionalized CNTs in an epoxy matrix. While un-functionalized CNTs showed less than a 10 % improvement on mechanical properties at 0.3 wt % loadings, a 0.5 wt % loading of

amine functionalized double-wall CNTs showed a 15 % increase in Young's modulus (from 2.59 GPa to 2.97 GPa), a 9 % increase in the ultimate tensile strength (from 63.80 MPa to 69.13 MPa) and a 43 % increase in the mode I fracture toughness (from 0.65 $MPa.m^{½}$ to 0.93 $MPa.m^{½}$).[26] Recently, Hsieh et al. reported an increase in fracture energy from 133 to 223 J/m^2 together with an enhanced fatigue performance in the form of an increased threshold strain-energy release-rate from 24 J/m^2 to 73 J/m^2 upon addition of 0.5 wt % of MWCNTs to an anhydride-cured epoxy.[27]

Electrically percolating CNT networks in polymers show typical conductivities ranging from 10^{-2} to 10^{3} S/m and percolation thresholds ranging from 0.1 to 2 wt %. Sandler et al. showed that sufficient conductivity for anti-static applications can be attained at a CNT loading of 0.005 wt %. In this work, aligned MWCNTs were produced by chemical vapor deposition followed by dispersion of the nanotubes in the epoxy resin via a shear-intensive processing. At a loading fraction of 1 wt %, the value of the electrical conductivity was 2 S/m, much lower than the intrinsic conductivity of CNTs. This observation was explained on the basis of a hopping electron transfer mechanism. Electron hopping between individual nanotubes and bundles of nanotubes is necessary due to the absence of direct contact between nanotubes in the presence of the polymer matrix.[28]

1.3. Graphene

Graphene is a molecular sheet one carbon (C) atom thick. Graphene sheets are made, primarily, of sp^2-hybridized C atoms arranged in a honeycomb structure where each C atom is covalently bonded to three other C atoms as illustrated in Figure 1-1. Graphene has a thickness around 0.3 nm and a size, corresponding to the lateral dimensions of the sheet, ranging from hundreds of nanometers to tens of microns. Graphene can present aspect-ratios of 100,000. Graphene is a non-stoichiometric compound; it presents a distribution of compositions, sizes and shapes. Therefore, the compositions of graphene and graphene derivatives are characterized in terms of average parameters such as the relative amounts of O and C atoms, or the relative amounts of functional groups.

The understanding of graphene properties has significantly advanced over the recent years thanks to the method reported by Novoselov et al. to exfoliate individual sheets directly from graphite.[29] Graphene has an intrinsic charge carrier mobility at room temperature of 200,000 cm^2/Vs, higher than any other known material. This makes graphene an excellent conductor of electricity. The upper bound of electrical conductivity enhancement that graphene sheets could bring to polymers is expected to be the in-plane conductivity or conductivity along the a-axis of highly oriented pyrolytic graphite (HOPG), this is $2.5x10^6$ S/m.[30, 31] Graphene has an elastic modulus of 1 TPa and a tensile strength of 130 GPa.[32] In addition to the good electrical and mechanical properties, which are similar to those found in CNTs, graphene has good barrier properties. Bunch et al. showed that graphene is impermeable to gases by applying a pressure difference across one sheet.[33]

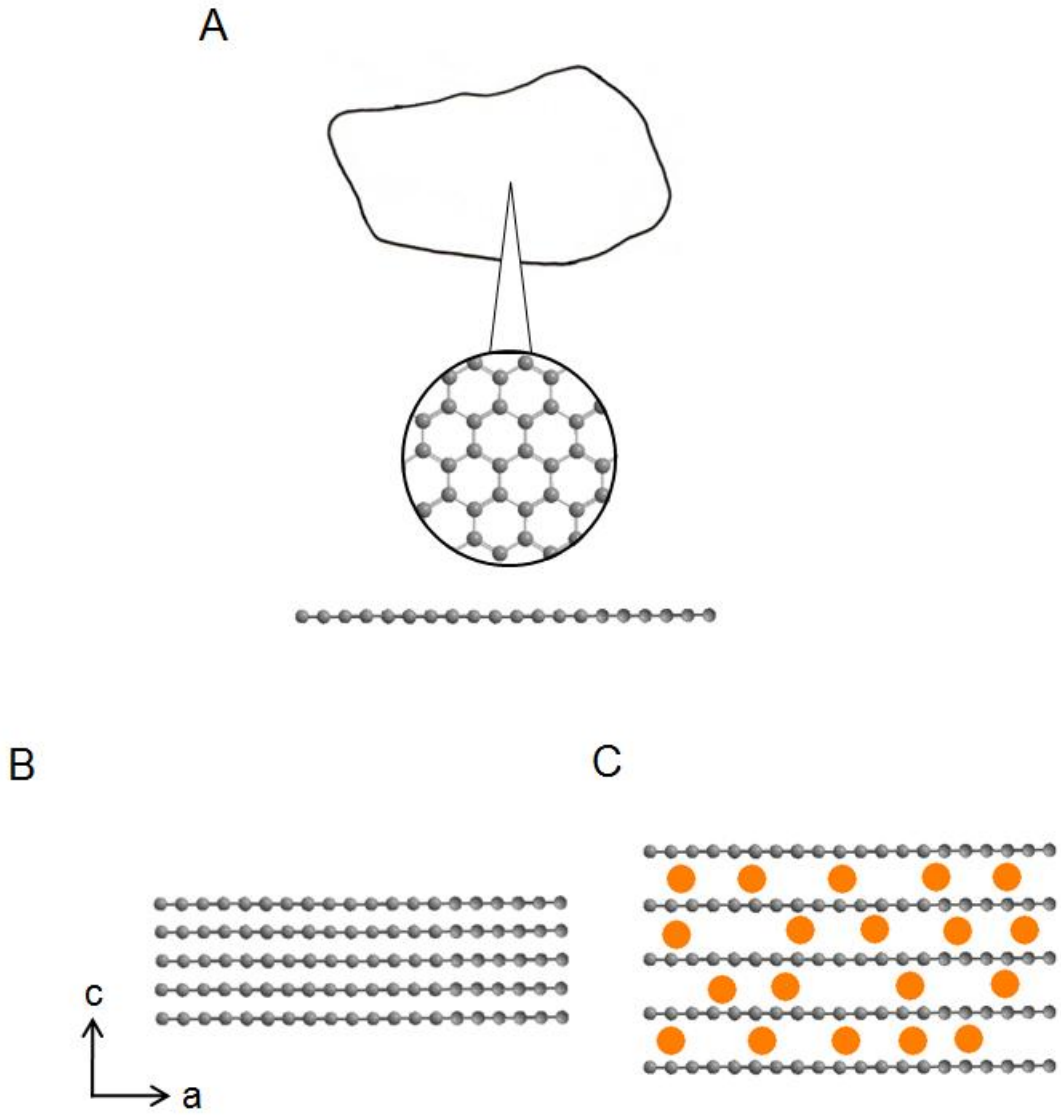

Figure 1-1. Schematics of the (A) arrangement of C atoms in graphene, top-view (top) and edge-view (bottom), (B) layered structure of graphene sheets in graphite as seen along the [1,2,0] zone axis and (C) structure of stage 1 graphite intercalation compound.[34]

Graphene has a unique combination of electrical, mechanical and barrier properties.[35] It is therefore of interest to use graphene as additive for polymers. In order to do so, it is required to exfoliate graphite in bulk quantities and to disperse the exfoliated graphene sheets in the polymer or pre-polymer resins. Two main routes exist to exfoliate graphite, the graphite oxide and the expanded graphite route. Chapter 2 reviews these two graphite exfoliation routes and presents a new processing method to prepare graphene-epoxy nanocomposites.

Chapter 2

Processing method for graphene-epoxy nanocomposites

This Chapter is organized into 3 sections. The first section reviews the graphite oxide and expanded graphite routes to exfoliate graphite. The second section describes the method proposed to prepare graphene-epoxy nanocomposites. The third section reports the analysis of the graphene sheets along the processing stages.

2.1. Introduction

Typical graphite flakes are made of thousands of stacked graphene sheets. In order to disperse the sheets in a polymer matrix, it is necessary to exfoliate the flakes. There exist two main routes to exfoliate graphite, one is based on the oxidation of graphite to graphite oxide and the other is based on the thermal expansion of intercalated graphite.

Expanded graphite is a form of graphite where the interlayer distance between some of the sheets has increased causing an expansion of the flakes along their thickness. Expanded graphite is prepared by thermal shock around 800 °C to 1000 °C of intercalated graphite, see Figure 1-1-C. Sulfuric acid is a commonly used intercalant in the production of expandable graphite. At high temperatures, the decomposition of sulfuric acid molecules results in formation of gas molecules such as H_2O, SO_3, SO_2, and O_2 causing a rapid volume expansion that splits some of the sheets apart.[36]

Sonication can break the expanded graphite flakes down into thinner flakes. Chen et al. reported typical thicknesses of sonicated expanded graphite ranging from 30 nm to 80 nm.[37] Yasmin et al. studied an epoxy filled with this type of thin graphite flakes. At a loading of 1 wt %, the nanocomposites showed higher elastic modulus, with increments up to 15 %, but lower tensile strength compared to the neat epoxy resin.[38] Lee et al. reported an enhanced electrical conductivity using nitric acid treated thin graphite flakes. A conductivity of 10^{-2} S/m was reported at 0.5 vol. % (0.9 wt %, assuming a density for graphite of 2.2 g/cm3 and a

density of 1.2 g/cm3 for the epoxy matrix), compared to a 2 vol. % (3.6 wt %) loading required when using thicker un-treated graphite flakes.[39]

Under severe oxidative conditions, graphite can be oxidized to graphite oxide. Graphite oxide is made of graphene oxide (GO) sheets; this is a form of graphene where oxygenated functional groups are covalently attached to the C atoms in the sheets. GO contains hydroxyl, epoxy, carbonyl and carboxylic acid groups covalently bonded to some of the C atoms.[40] The C to O ratio in GO ranges from 1.5 to 3. Oxidation of graphite to graphite oxide can be monitored with XRD. Typically, the disappearance of the 0.34 nm interlayer spacing of graphite is observed jointly with the appearance of a new broader diffraction peak at lower angles corresponding to a higher interlayer spacing. Hennig reported interlayer spacings in graphite oxide ranging from 0.6 to 1.1 nm depending on the C to O ratio.[41] This increase in interlayer spacing is related to the increase in the thickness of the sheets due to the addition of O functional groups.

GO sheets can contain un-oxidized regions where C atoms have the same chemical structure as in the original graphene sheets. These regions are labeled graphene regions and the fraction of graphene regions is defined as the graphene content of the sheets. Thus, GO sheets have a heterogeneous chemical composition composed of graphene regions and functionalized (oxidized) graphene regions. The work by Wilson et al. on advanced electron imaging and diffraction analysis of GO supports this heterogeneous structural picture of the sheets.[42]

Several methods have been reported to prepare graphite oxide. Brodie's method consists in reacting graphite with fuming nitric acid and alkali chlorate.[43] The method of Hummers and Offeman involves the reaction of graphite with sodium nitrate in sulfuric acid followed by permanganate oxidation.[44]

Graphite oxide readily exfoliates in water into stable dispersions of GO sheets. GO sheets have a negatively charged surface in water. The high stability of GO dispersions in water has been explained in terms of an electrostatic repulsion between the sheets. Li et al. reported zeta-potential measurements on aqueous dispersions of GO showing that the surface charge is pH dependent.[45]

The oxidation of graphene breaks the conjugated network of sp^2-hybridized C atoms which results in a loss of electrical conductivity. Hennig reported an electrical conductivity of 10^{-5} S/m at a C to O ratio of 3.[46]

While the graphite oxide route enables a better exfoliation of the flakes than the expanded graphite route, the resulting GO is highly oxidized and has poor electrical conductivity. Therefore, additional treatments are required to reduce GO in order to recover the electrical properties of graphene and have sufficient electrical conductivity to avoid static charge buildup, for example.

The chemical reduction of GO recovers part of the electrical properties of graphene. Boehm et al. reported the use of alkaline conditions to reduce GO.[47] Stankovich et al.

prepared GO following the Hummers and Offeman's method and then reduced GO with hydrazine hydrate following Boehm's method,[48] resulting in a compressed powder of reduced GO with a C to O ratio of 10.3 and electrical conductivity of $2x10^2$ S/m.[49] In another work, Stankovich et al. prepared reduced GO filled polystyrene. The conductivity of the polystyrene nanocomposites was 10^{-1} S/m at 1 vol. % (2.2 wt %, assuming a density for graphite of 2.2 g/cm^3 and a density for polystyrene of 1 g/cm^3), and the percolation threshold was 0.1 vol. % (0.22 wt %).[50]

Upon heating oxygenated functional groups are removed from GO by thermolysis. Brodie reported that oxidized graphite is thermally unstable and that its thermal decomposition results in loss of O.[51] Croft reported the onset of thermal decomposition in graphite oxide at temperatures as low as 70 °C.[52]

Depending on the heating rate the thermal decomposition of oxygenated functional groups in graphite oxide can result in vigorous release of gases yielding an expansion of the flakes similar to the process followed to prepare expanded graphite. Schniepp et al. applied heating rates above 2,000 °C/min to graphite oxide up to 1,050 °C. The resulting material showed a 500 to 1,000 times volume expansion and surface areas ranging from 700 to 1,500 m^2/g. The theoretical specific surface area of a graphene sheet is 2,630 m^2/g. Thermal-shock reduced GO sheets presented a C to O ratio of 10 and had an average thickness of 2 nm. The sheets were dispersed in a water soluble poly(ethylene glycol)-block-poly(propylene glycol)-block-poly(ethylene glycol) surfactant resulting in films with conductivities of 10^3 S/m.[53]

Exfoliated GO has excellent exfoliation stability in water. Reduction in water is preferable in order to maintain a high degree of exfoliation. Prior methods to reduce GO in water present the following shortcomings. Reported methods have made use of hazardous chemicals such as hydrazine that are not suitable components in polymer formulations. Further, the potential aggregation of GO after reduction requires the use of stabilizers such as surfactants which may not be suitable components in polymer formulations. Filtration steps may also be required. Filtering exfoliated graphene dispersions is not scalable to large volumes. Because of the excellent barrier properties of graphene, exfoliated graphene dispersions rapidly plug filters, slowing down filtration to unprofitable rates and/or requiring vacuum systems which add to the cost. Other drawbacks include the use of organic solvents, the use of sonication steps and the use of high temperatures.[54]

There is a need for innovative processing methods to prepare graphene-polymer nanocomposites. The following section reports a new processing method to reduce GO in water and to transfer the reduced GO out of the water phase into a pre-polymer phase suitable for compounding epoxy formulations.

2.2. Processing method

The method to prepare graphene epoxy nanocomposites consists of the following steps:

(1) Preparation of GO

(2) Modification of GO with isophorone diamine (IPDA)

(3) Formation of the liquid foam of graphene (LFG)

(4) Mixing of the foam with IPDA and dehydration

(5) Compounding and curing

2.2.1. Preparation of graphene oxide

The synthesis of GO followed the method of Hummers and Offeman.[55] The synthesis was conducted in an open glass reactor and using de-ionized water. Figure 2-1 is a scanning electron microscope (SEM) image of the graphite flakes. 10 g of graphite were added to a 400 ml 96 wt % aqueous solution of sulfuric acid containing 5 g of sodium nitrate (≥ 99 %) under stirring and cooled in an ice bath. Then 30 g of potassium permanganate (99 %) were added to the mixture. After the addition of potassium permanganate, the reaction was left stirring for 2 h. Then the reactor was removed from the ice bath and immersed in a water bath at 23 °C. The reaction was left under stirring for 4 days to a total of 5 days.

After 5 days, the reaction became a dark grey/violet paste. The paste was then added into 1 liter of water containing 5 wt % of sulfuric acid. The residual permanganate was then neutralized with a 30 wt % aqueous solution of hydrogen peroxide until the mixture turned yellow. The mixture was then poured into 1 liter of water containing 5 wt % of sulfuric acid and 1 wt % of hydrogen peroxide.

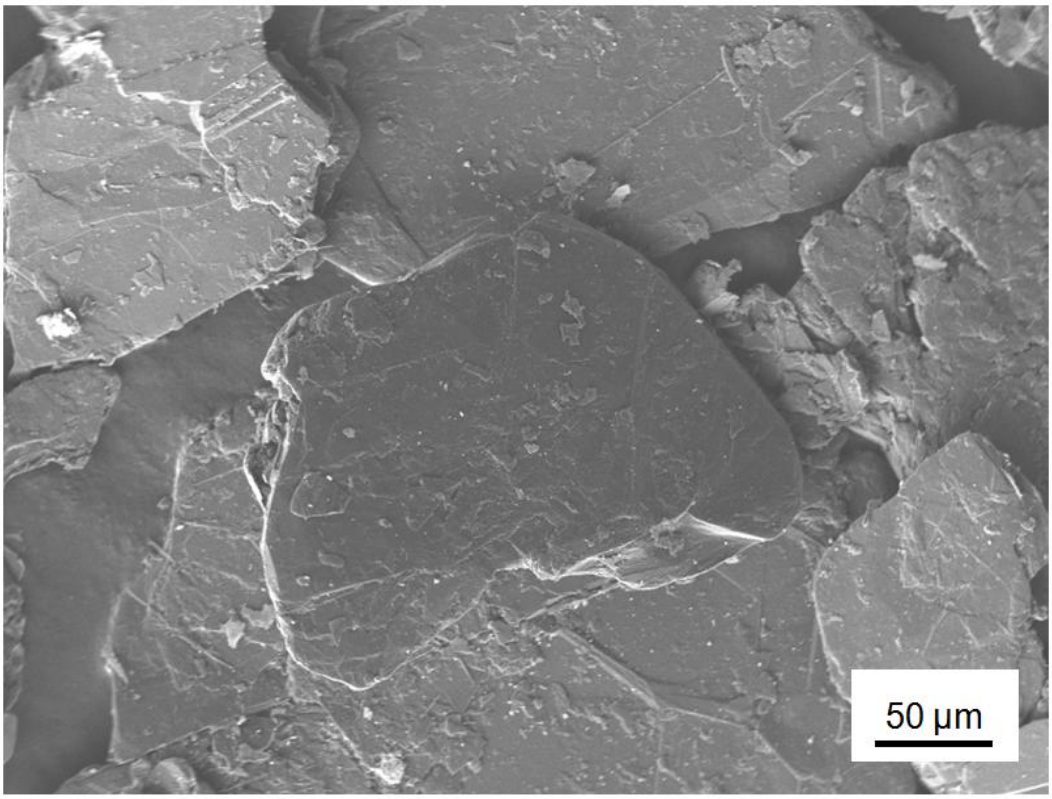

Figure 2-1. SEM of the graphite flakes. Graphite flakes were deposited on a double-sided conductive carbon tape attached to an aluminum sample holder.

The product was centrifuged, the supernatant was discarded and the deposit was dissolved again in an aqueous solution containing sulfuric acid (5 wt %) and hydrogen peroxide (1 wt %). This cycle was repeated a total of 5 times. Then the same cycle was conducted using an aqueous solution containing 4 wt % of hydrochloric acid until the supernatant tested negative for sulfates. The final deposit was dispersed in water to yield a 0.5 wt % dispersion of GO. An atomic force microscope (AFM) analysis of one of the GO sheets is shown in Figure 2-2.

2.2.2. Modification of graphene oxide with isophorone diamine

The chemical structure of IPDA (5-Amino-1,3,3-trimethylcyclohexanemethylamine, CAS # 2855-13-2) is shown in Figure 2-3. The reaction of GO with IPDA consisted of the following steps. Equal volumes of GO in water and IPDA, for example, 50 ml of 0.5 wt % of GO in water and 50 ml of IPDA (≥ 99 %) were mixed in a glass beaker, and then the reaction was left under stirring during 24 hours at 23 °C.

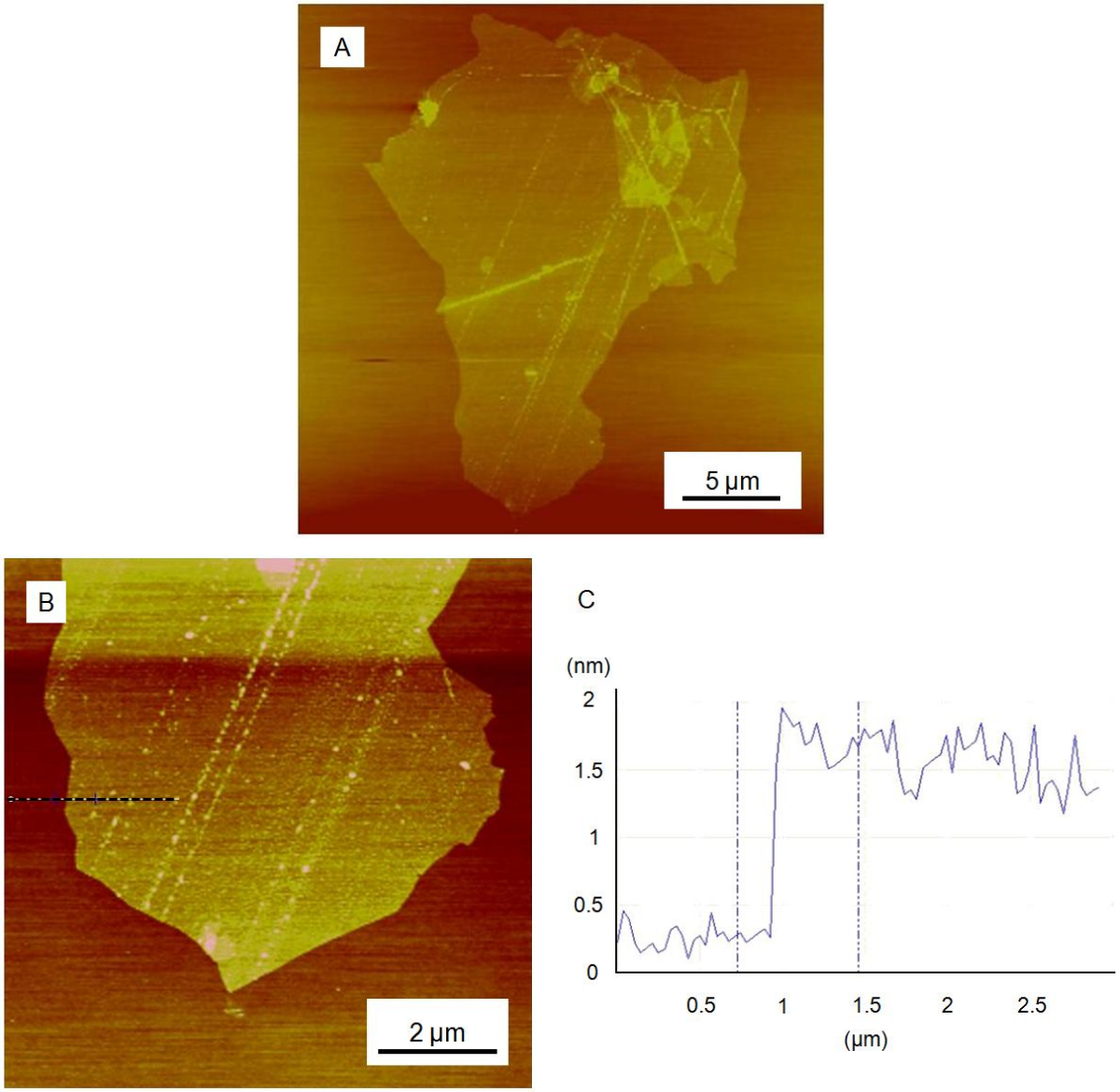

Figure 2-2. (A and B) AFM tapping mode image of a GO sheet on a silicon substrate. B is a magnified image of the bottom region in A. (C) The thickness of the sheet is measured at the edge of the sheet along the line shown in B. The sheet is about 1 nm thick. Sample preparation consisted in drop casting an aliquot of an aqueous dispersion of GO sheets on a silicon wafer with a 300 nm layer of silicon oxide.[56] Then the sample was dried in a dessicator under a vacuum of 10 Pa during 24 h.

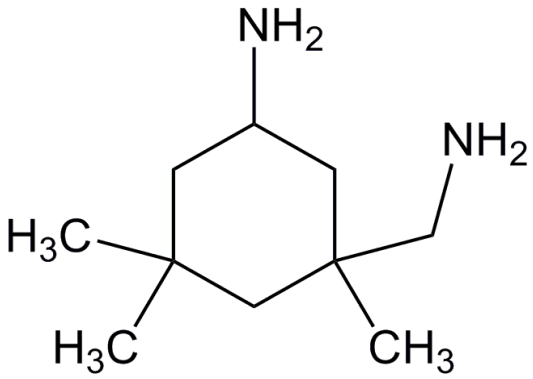

Figure 2-3. Chemical structure of IPDA.

2.2.3. Formation of the liquid foam of graphene

To extract the IPDA modified GO sheets out of the reaction product, an excess of water was added to the mixture and then the mixture was agitated to produce a foamed phase. The analysis of the LFG is reported in the next chapter.

An example of this step follows; 4 ml of the product of the previous step were mixed with 10 ml of de-ionized water. After agitating the mixture in a closed vial, a foam spontaneously formed. Removal of the foam from the water surface was done by skimming the foam off.

2.2.4. Mixing of the foam with isophorone diamine and dehydration

The foam was mixed with IPDA and the mixture was heated following a distillation process. IPDA has a boiling point of 247 °C. No literature was found reporting an azeotrope between IPDA and water.

The distillation equipment consisted of a round-bottom glass flask, where the mixture was heated, connected to a still head equipped with a thermometer. The still head was connected to a condenser and the condenser was connected to a still receiver that conducted the distillate into a receiving flask. A silicone bath was used to provide homogeneous heating.

An example of this step follows; 6.4 g of foam were mixed with 25.4 g of IPDA in a glass beaker. Then the mixture was transferred to a round-bottom flask which was connected to a distillation set-up and then immersed in a silicone bath. The mixture was heated following the temperature program shown in Table 2-1. The heating rate was on average 5 °C/min from 31 °C to 200 °C. The mixture was kept at 200 °C during 20 minutes. After completing the temperature program, the round-bottom flask was removed from the silicone bath. The amount of water in the foam, corresponding to the distilled fraction collected at a distillation temperature of 100 °C, was 5.43 g corresponding to 85 % of the foam in mass. This corresponds to a loading of 3.8 wt % of sheets in the dehydrated product.

Time (min.)	Bath Set (°C)	Bath Actual (°C)	Distillation Thermometer (°C)
0	150	31	23
10	150	135	23
20	200	149	100
30	200	186	100
40	200	200	100
50	200	200	70
60	200	200	50

Table 2-1. Temperature program followed during the dehydration step.

2.2.5. Compounding and curing

The dehydrated product was mixed with the remaining of the epoxy formulation. In the epoxy system used the hardener part contains up to 60 % by weight of IPDA as shown in Table 2-2.

The following is an example of the steps followed to compound the thermosetting formulation. 1 g of the dehydrated product was placed in a glass vial, and then 2.57 g of epoxy resin were added to the vial. Mixing was done with a spatula. The loading of graphene sheets in this particular nanocomposite formulation was 1 wt %. A vacuum of 10 Pa was applied during 10 minutes to de-aerate the mixture before curing.

Curing was conducted following the thermal cycle shown in Table 2-2. An example of the curing process follows. The de-aerated mixture was left at 23 °C during 24 h. Then, the sample was placed in an oven at 100 °C. After 4 hours, the sample was removed from the oven.

Resin Part	Composition	Chemical structure	Mix Ratio	Cure Cycle
Araldite LY 5052 epoxy resin	Butanediol diglycidyl ether (15 - 40 wt %)		100	1 day at 23 °C followed by 4 h at 100 °C
	Epoxy phenol Novolac (40 - 70 wt %)	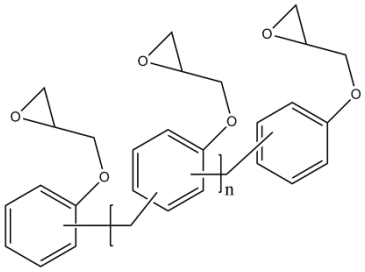		
Aradur 5052 CH mixture of polyamines curing agent	IPDA (30 - 60 wt %)	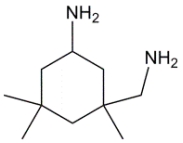	38	
	Cycloaliphatic diamine (30 - 60 wt %)	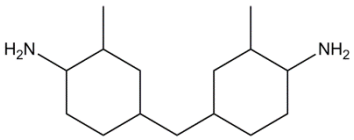		

Table 2-2. Epoxy system.

2.3. Analysis of the graphene sheets along the processing stages

This section is organized in 4 sub-sections. The first sub-section gives an overview of the processing method and summarizes the main conclusions drawn from the analysis of the sheets. Each one of the following 3 sub-sections covers the x-ray photoelectron spectroscopy (XPS), the XRD and the transmission electron microscope (TEM) analysis separately.

The following nomenclature is used to label the graphene sheets:

(1) Graphene. These are the sheets in the graphite flakes.

(2) GO. These are the oxidized sheets.

(3) Modified GO (foam): MGO (foam). These are the sheets that make the foam.

(4) Modified GO (nanocomposite): MGO (nanocomposite). These are the sheets in the nanocomposite.

2.3.1. Overview

The graphene sheets undergo several chemical modifications along the processing stages. Initially, graphite flakes are oxidized to graphite oxide. The resulting GO sheets are dispersed in water forming stable dispersions as shown in Figure 2-4-A. Then GO is chemically modified with IPDA. The product of the reaction between GO and IPDA in water is shown in Figure 2-4-B. The resulting MGO (foam) is extracted from the reaction product in the form of a liquid foam as illustrated in Figure 2-4-C. The foam is skimmed off the liquid surface and then mixed with IPDA. Then, the mixture undergoes a distillation process to remove the water. The dehydrated mixture containing MGO (nanocomposite) in IPDA is shown in Figure 2-4-D. Finally, the dehydrated mixture is compounded with the rest of the epoxy formulation and cured to yield a nanocomposite with a homogeneous dispersion of MGO (nanocomposites) sheets in the epoxy matrix as shown in Figure 2-5.

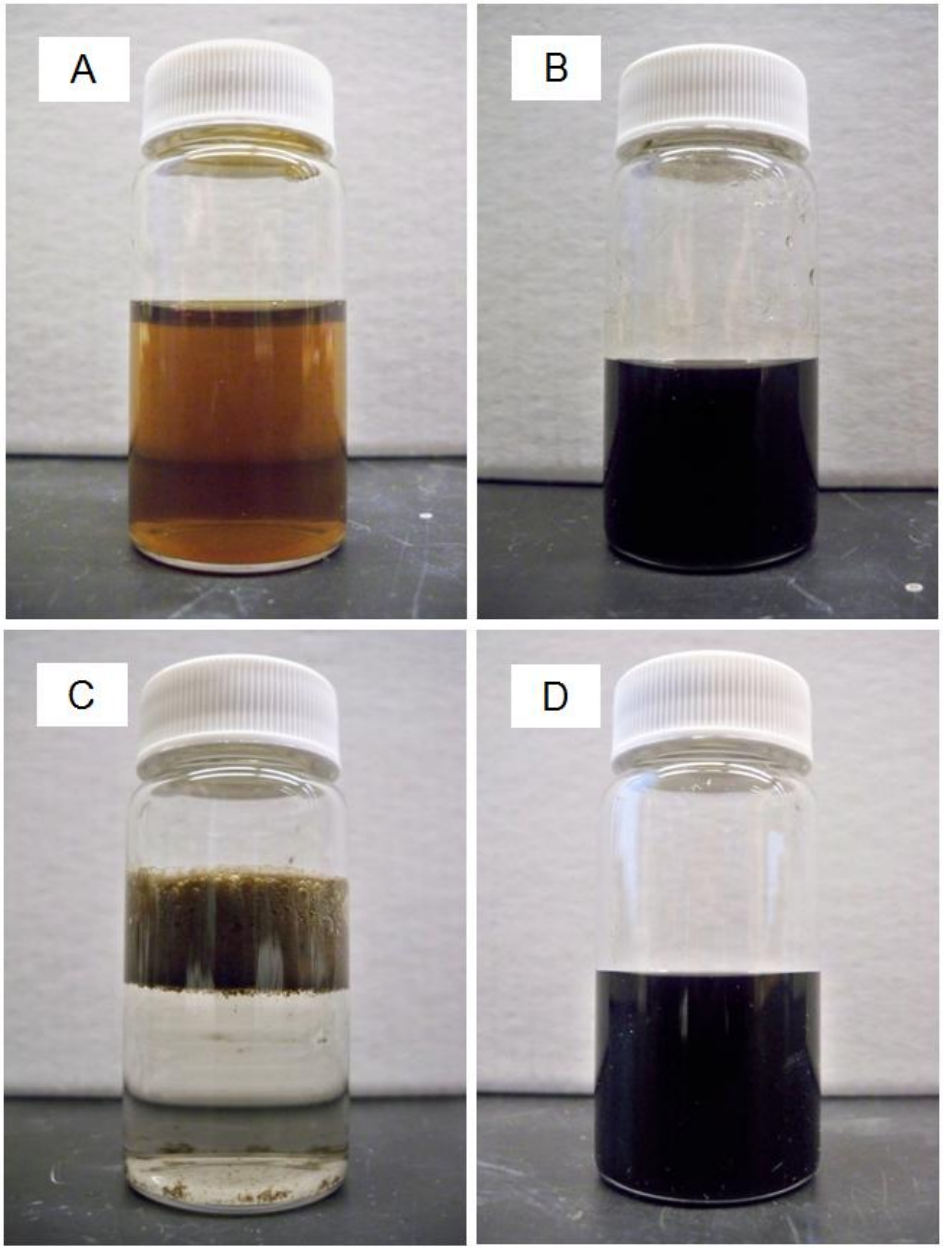

Figure 2-4. Representative stages of the processing method. (A) GO in water, (B) product of the reaction between GO and IPDA in water, (C) liquid foam extraction of MGO (foam) and (D) dehydrated dispersion of MGO (nanocomposite) in IPDA.

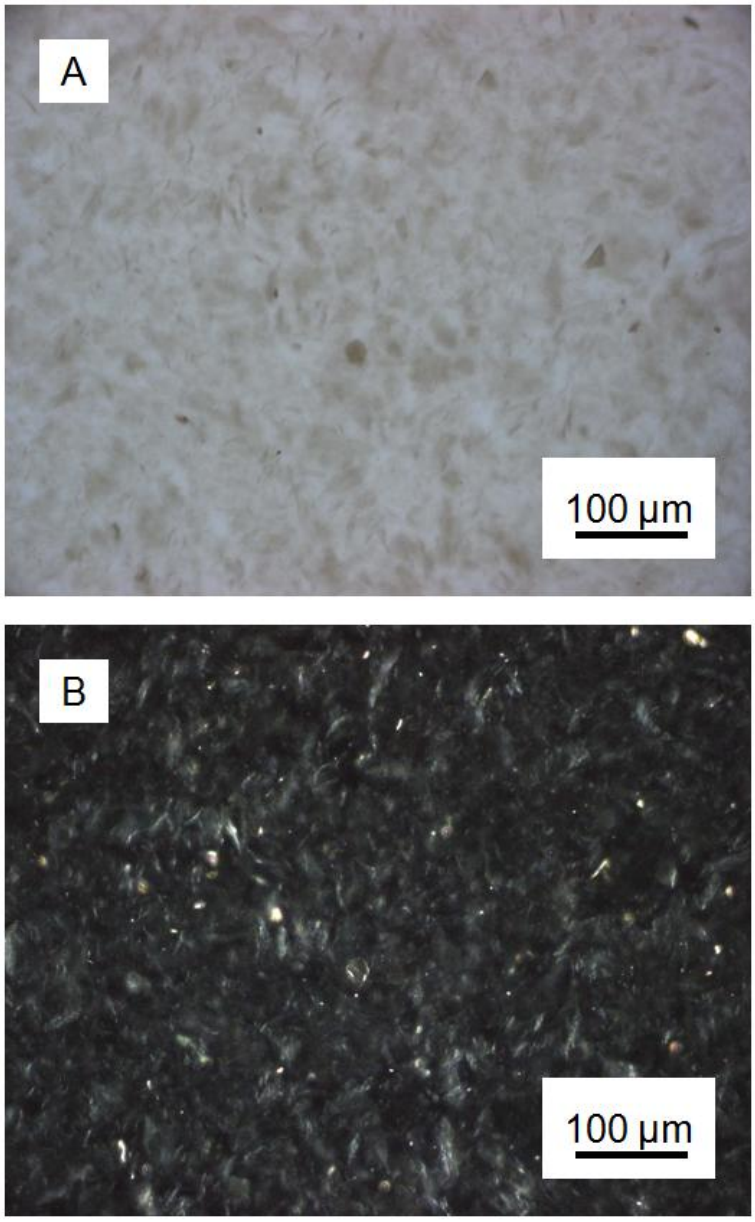

Figure 2-5. (A) Transmission light microscope image of the dispersion of MGO (nanocomposite) sheets in the epoxy matrix. (A). (B) Imaging between crossed-polars. An aliquot of the uncured mixture of graphene epoxy nanocomposite was deposited between glass slides. Then the mixture was cured. The sample consists in a sandwich of cured graphene-epoxy nanocomposite between glass slides.

The changes in the chemical composition of the graphene sheets along the processing stages are summarized in Figure 2-6. The oxidation of graphene to GO results in a C to O ratio of 3. High-resolution XPS analysis of the C 1s region shows that the 16 atomic % of C atoms in GO belong to graphene regions. The rest of C atoms that make up the GO sheets are saturated hydrocarbons and C atoms covalently bonded to oxygenated functional groups. Figure 2-6-B illustrates the 5 types of C chemistries present in the functionalized graphene regions in GO, namely the hydroxyl, epoxy, carboxylic, carbonyl and hydrocarbon chemistries. The presence of 0.7 atomic % of N atoms in GO is attributed to the nitrates used during the oxidation step. TEM analysis of the sheets confirms the presence of crystalline graphene regions in GO as well as in the modified forms of GO. Figures 2-6-C and D take into account the incorporation of N atoms in the functionalized graphene regions in the form of an additional C chemistry that adds up to a total of 6 C chemistries.

A 10 wt % aqueous solution of IPDA has a pH of 12. IPDA provides the alkaline condition that reduces GO. Reduction in chemistry means a gain in electrons. Here, the term reduction is used more specifically to indicate an increase in graphene content of the sheets. In MGO (foam), the C to O ratio increases from 3 to 4.1. The graphene content increases from 16 atomic % to 38.2 atomic %, this corresponds to a reduction of 22.2 % of C atoms in GO back into sp^2-hybridized networks. In addition to reducing GO, the reaction with IPDA incorporates N atoms to the sheets. A total of 3.1 % of atoms in MGO (foam) are N atoms.

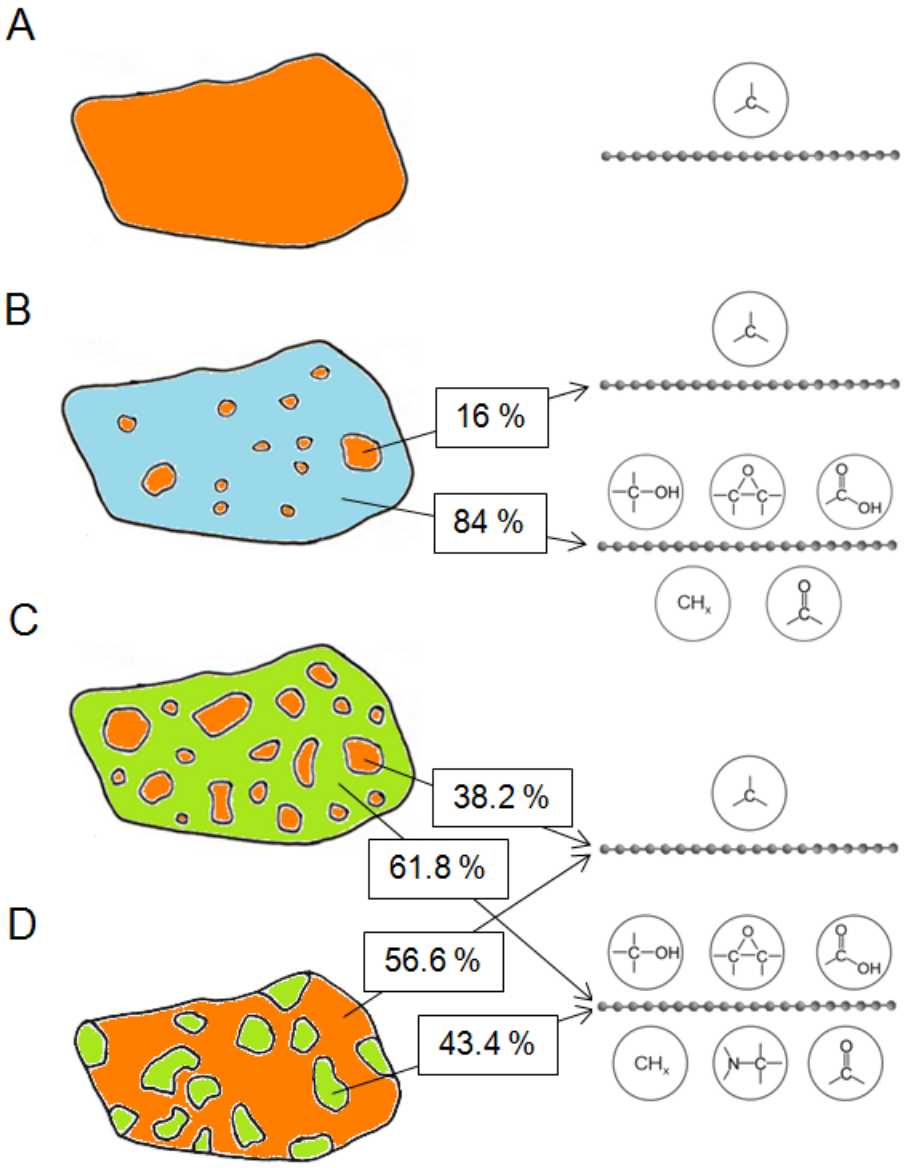

Figure 2-6. Evolution of the chemical make-up of the graphene sheets. (A) Graphene, (B) GO, (C) MGO (foam), (D) MGO (nanocomposite). Left, view normal to the plane of the sheets illustrating the heterogeneous distribution of graphene regions and functionalized graphene regions. Right, edge-on view of the sheets indicating the types of C chemistries present in each one of the regions. Percentages correspond to atomic % of C atoms based on XPS analysis.

The dehydration step involves heating the mixture of MGO (foam) and IPDA up to 200 °C. Heating the sheets at 200 °C in the presence of IPDA further reduces and functionalizes the sheets. MGO (nanocomposite) presents a C to O ratio of 16.3 and a 56.6 atomic % of graphene content, corresponding to an additional 18.4 atomic % reduction of C atoms. The N content doubled to 6.2 atomic %. IPDA is the only possible source of N atoms to account for the increase in N content in the modified forms of GO. The IPDA molecules incorporate into the structure of the sheets. In addition to functionalize GO, IPDA provides the alkaline condition that reduces the sheets. In MGO (nanocomposites) heating further reduces the sheets.

The thickness of the sheets gradually increases from graphene to MGO (nanocomposite). XRD analysis shows that the interlayer spacing in crystallites made of stacks of sheets increases from 0.34 nm in graphene to 0.79 nm in GO, to 1.14 nm in MGO (foam) and finally to 1.34 nm in MGO (nanocomposite). The crystallization of the sheets shows a gradual decrease in the number of sheets per crystallite which is attributed to a higher dispersion in sheet thickness. An increase in the roughness of the sheets due to the heterogeneous incorporation of IPDA molecules to the sheet structure is the possible source of the increasing thickness dispersion. TEM analysis of the sheets supports the explanation of a gradual increase in surface roughness due to the functionalization of the sheets with IPDA, visible in MGO (nanocomposite) as a coating.

The surface chemistry of the sheets changes from hydrophilic in GO to hydrophobic in the modified forms of GO. GO is a hygroscopic material. Freeze-dried powders of GO

quickly uptake ambient moisture. XRD analysis shows an increase in interlayer spacing in GO crystallites when measurements are conducted on unsealed samples compared to measurements conducted on sealed samples. This interlayer spacing increase from sealed to unsealed samples is not observed in any of the modified forms of GO. Furthermore, MGO (foam) films show a static contact angle of 109 ±12°. In contrast, GO films swell the drop of water forming a bump. The contact angle observed in MGO (foam) is higher than 90° indicative of the hydrophobic character of the sheets.

2.3.2. X-ray photoelectron spectroscopy

XPS is used to quantify the elemental composition and C chemistries present in the sheets. This enables monitoring the chemical modification of the sheets along the processing stages.

The basic equation of XPS is the one describing the photoelectron emission process

$$E_k = h\nu - E_B - \phi$$

where E_k is the measured kinetic energy of the ejected electron, $h\nu$ is the energy of the exciting photons, E_B is the binding energy of the electron in the material, and ϕ is the work function, a catch-all term whose precise value depends on the sample and the instrument. A calibration in terms of an energy referencing is required in XPS analysis.

The energy referencing strategy used is based on the assumption that all the sheets contain graphene regions where the C atoms have the chemical structure found in graphene and that this chemical state of C corresponds to the lowest possible binding energy for C in the sheets. Based on this assumption, all the high-resolution spectra are shifted such that the lowest binding energy component in the C 1s peak decomposition is centered at 284.4 eV. This is the binding energy of C in graphite.[57] TEM diffraction analysis of GO and the modified forms of GO confirms the presence of graphene regions in all the sheets supporting the energy referencing strategy chosen.

The binding energy of saturated hydrocarbons is the reference value commonly used if energy referencing is done with adventitious carbon. However, this energy referencing strategy has an uncertainty caused by the spread of values reported in the literature. Binding energies between 284.8 eV and 285.2 eV are typical.[58] In the present analysis, it is more convenient to take advantage of the presence of graphene regions as internal calibration for energy referencing.

The summary of the elemental composition of the sheets is reported in Table 2-3. Elemental compositions were calculated from the XPS survey spectra shown in Figure 2-7.

	Atomic concentration (%)			C to O ratio
	Carbon	Oxygen	Nitrogen	C/O
Graphene	95.4	4.7	-	20.5
GO	74.7	24.6	0.7	3
MGO (foam)	78.1	18.8	3.1	4.1
MGO (nanocomposite)	88.4	5.4	6.2	16.3

Table 2-3. Elemental compositions of the sheets.

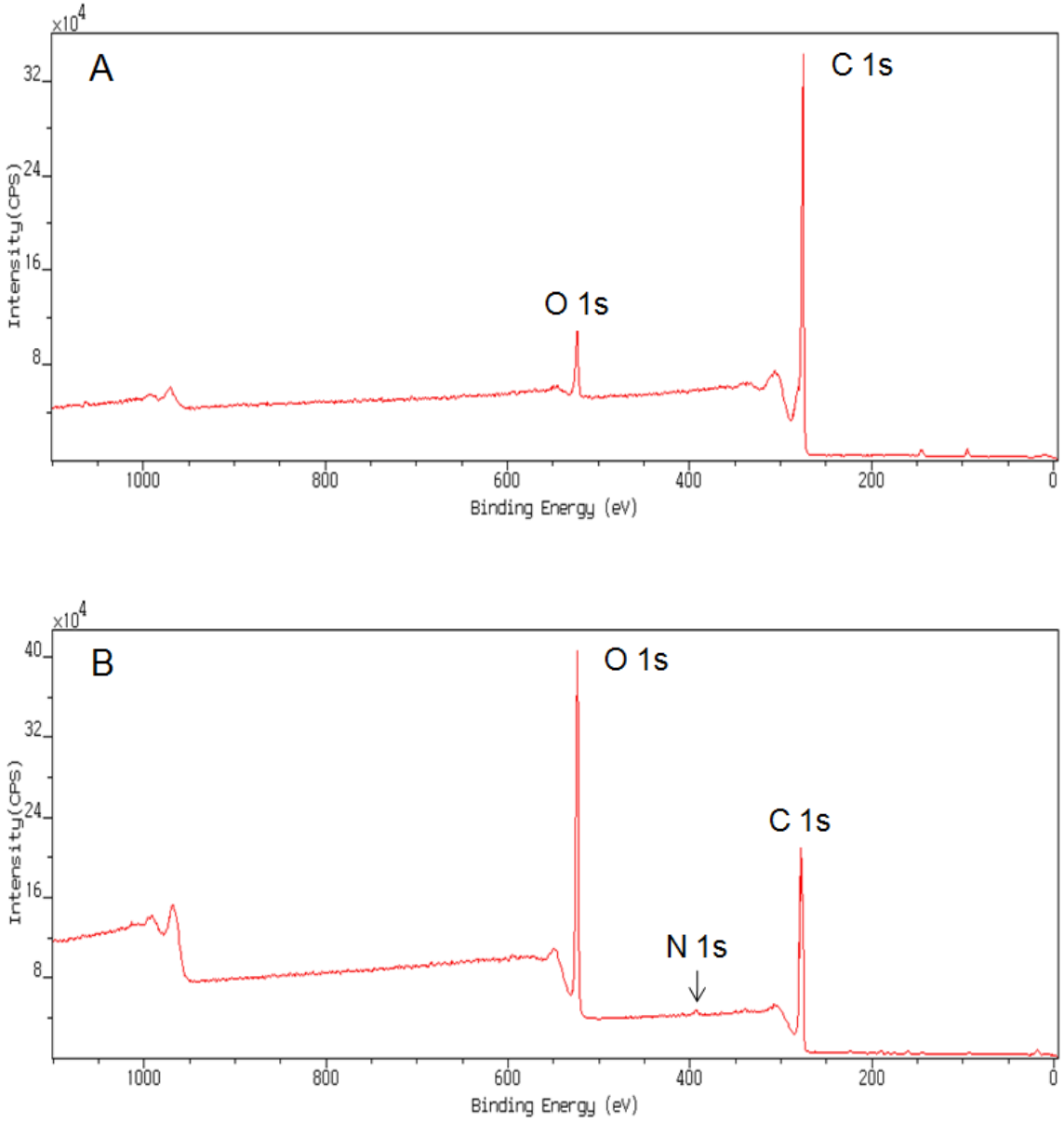

Figure 2-7. XPS survey spectra. (A) Graphene, (B) GO, (C) MGO (foam), (D) MGO (nanocomposite). CPS: Counts per second.

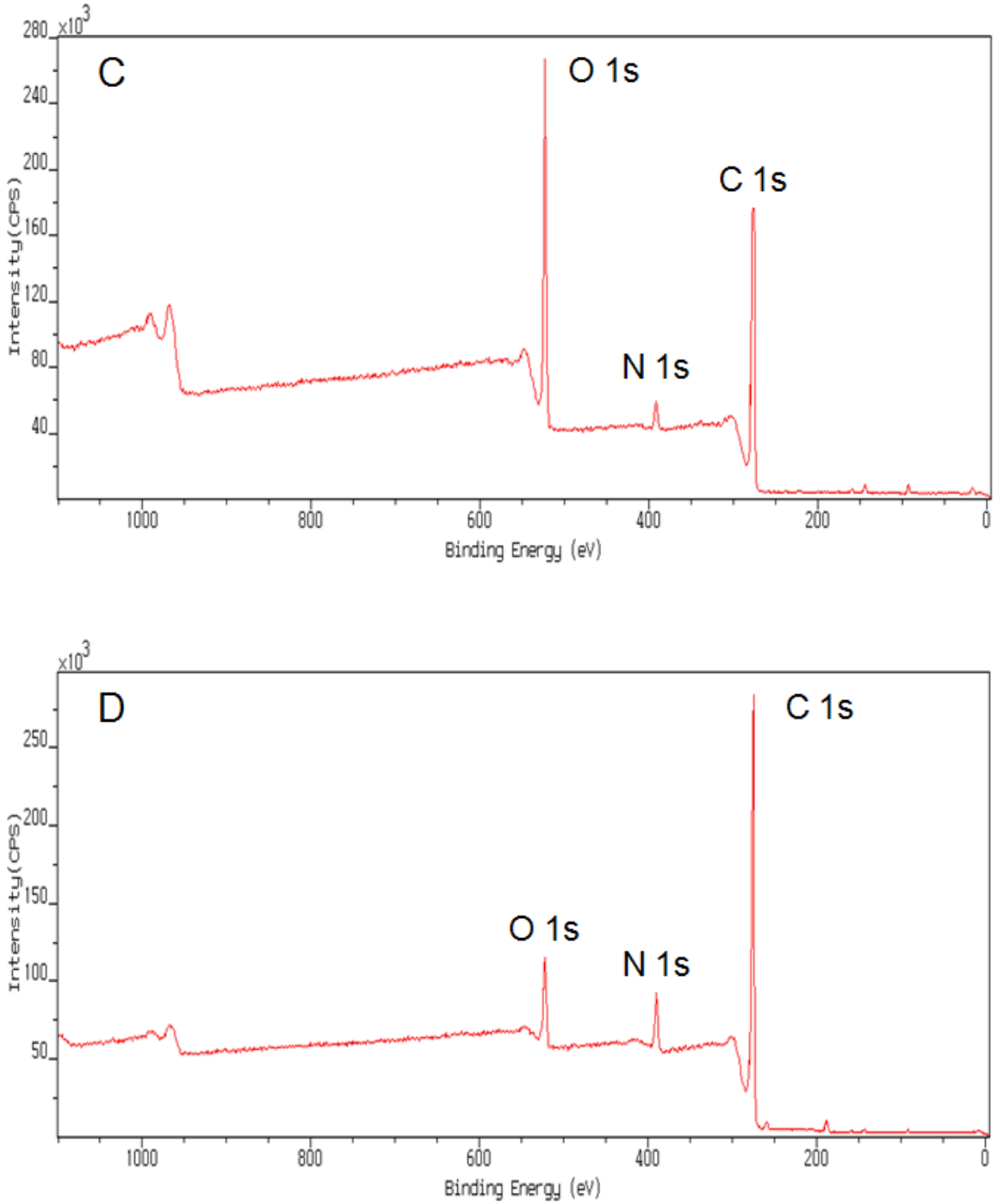

(cont.) Figure 2-7. XPS survey spectra. (A) Graphene, (B) GO, (C) MGO (foam), (D) MGO (nanocomposite). CPS: Counts per second.

The O content measured in graphite is attributed to a difference in composition between the skin and the core of the flakes. While the surface analysis provided by XPS is representative of the entire sample in GO and the modified forms of GO, this may not be the case for graphite. Sample preparation for GO and the modified forms of GO consisted in pressing freeze-dried powders of the sheets into films. The chemical composition of the sheets at or close to the surface of the films is then the same as that of the sheets at the interior of the films. Graphite is supplied in the form of flakes and the composition of the sheets at or close to the surface of the flakes may be different from the composition of the sheets at the interior of the flakes. During mining and processing, graphite undergoes potentially destructive processes such as milling that can oxidize the surface of the flakes.[59] The presence of N in GO is attributed to the use of sodium nitrate during the oxidation process.

High-resolution XPS is conducted to analyze the C chemistries present in the sheets. High resolution spectra of the C 1s region are shown in Figure 2-8. High-resolution spectra are obtained with an electron energy resolution of 0.25 eV. This level of resolution is enough to differentiate between functionalized and un-functionalized C atoms. This is shown by the presence of two shoulders in Figures 2-8-B and C. The right-hand shoulder corresponds to un-functionalized C atoms and the left-hand shoulder to functionalized C atoms. Figures 2-8-A and D present primarily un-functionalized C atoms. A higher resolution analysis of the C chemistries, for instance to differentiate among types of O functional groups linked to the C atoms, requires modeling the peak. Table 2-4 summarizes the C chemistries considered in modeling the decomposition of the C 1s peak.

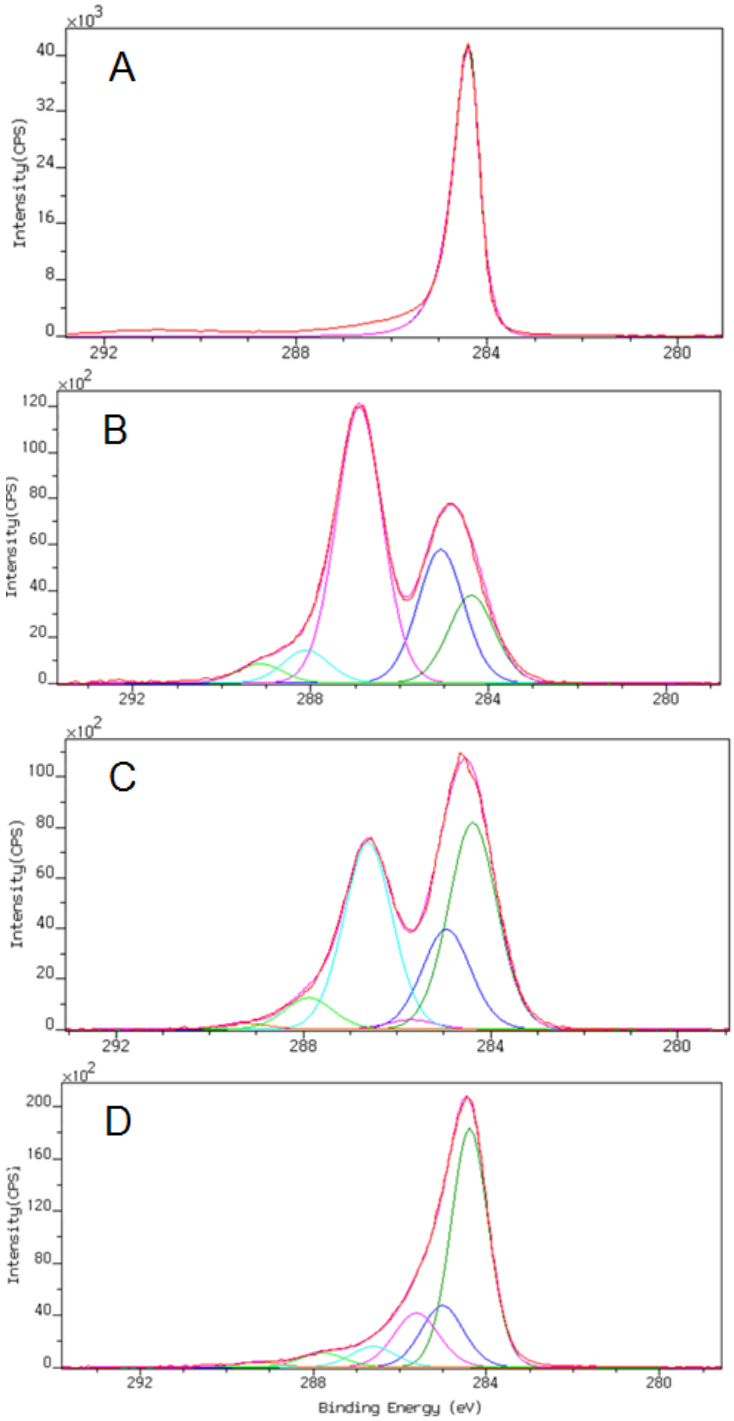

Figure 2-8. XPS high-resolution analysis of the C 1s region in (A) graphene, (B) GO, (C) MGO (foam), (D) MGO (nanocomposite). CPS: Counts per second.

Carbon chemistry		Binding energy (eV)
Graphene		284.4
Saturated hydrocarbon		285
Nitrogen	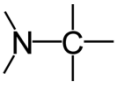	285.9
Hydroxyl & Epoxy	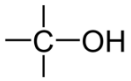 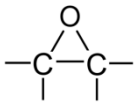	286.8
Carbonyl		287.9
Carboxylic	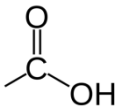	289.3

Table 2-4. Carbon chemistries and corresponding binding energies.

The decomposition of the C 1s peak is based on the following two assumptions. The first relates to the energy referencing strategy and the second to the type of functional groups expected in GO and in the modified forms of GO.

As discussed above, the presence of graphene regions in the sheets is used as internal calibration for energy referencing. The spectra are shifted such that the lowest energy component in the C 1s peak decomposition is centered at 284.4 eV. This corresponds to the binding energy of C in graphene. In addition to the component corresponding to graphene, another component is required to fit the right-hand shoulder. A component corresponding to C in saturated hydrocarbons is considered centered at 285 eV.

The presence of electron withdrawing atoms such as O atoms covalently bonded to C causes shifts to higher binding energies. As a rule of thumb, O induces shifts to higher binding energies by 1.5 eV per C-O bond. Starting at 285 eV for saturated hydrocarbons, carbons bearing hydroxyl and epoxy moieties would appear at 286.5 eV, carbonyl groups at 288 eV and carboxylic groups at 289.5 eV.[60]

In modeling the peak decomposition of the left-hand shoulder in GO, the following 4 oxygen functionalities are considered, hydroxyl, epoxy, carbonyl and carboxylic groups. Energy shifts relative to saturated hydrocarbon (C 1s = 285 eV) are used as a reference guide to position the components in the peak decomposition. The energy shifts are obtained from values found in polymers: + 1.55 eV (286.5 eV) hydroxyl, + 2.02 eV (287 eV) epoxy, + 2.90

eV (287.9 eV) carbonyl, and 4.26 eV (289.3 eV) carboxylic.[61] The contributions of C atoms with hydroxyl and epoxy groups are united into one peak component centered at 286.8 eV.

A component centered at 285.9 eV corresponding to C linked to N via a single bond is considered in modeling the left-hand shoulders in the modified forms of GO. This corresponds to a chemical shift relative to saturated hydrocarbon of +0.94 eV.

The graphene content is determined from the lowest energy peak component centered at 284.4 eV. Table 2-5 summarizes the evolution of the graphene content; graphene content increases from 16 atomic % in GO, to 38.2 atomic % in MGO (foam), and to 56.6 atomic % in MGO (nanocomposite). XPS analysis shows that the modified forms of GO are reduced forms of GO.

	C to O ratio	Graphene content (atomic %)
GO	3	16
MGO (foam)	4.1	38.2
MGO (nanocomposite)	16.3	56.6

Table 2-5. Summary of the gradual reduction of the sheets along the processing stages based on XPS analysis.

Each one of the XPS high-resolution analyses is reported below separately. The binding energy shifts reported in Tables 2-6 to 2-8 are calculated with respect to the binding energy in saturated hydrocarbons as it is typical in the literature since most measurements use adventitious carbon for energy referencing.

The XPS survey spectra show an increase in N content from 0.7 atomic % in GO, which is attributed to the nitrates used during the oxidation of graphite, to 3.1 atomic % in MGO (foam) and to 6.2 atomic % in MGO (nanocomposite).

XPS high resolution spectra show the presence of N atoms covalently bonded to C in the modified forms of GO. However, the XPS analysis is not conclusive with regard to whether these covalent C-N bonds are between the N in IPDA and C atoms in the sheet skeleton, or rather, they are C-N bonds in IPDA molecules attached to the sheets via non-covalent bonding. A more thorough study would be necessary to elucidate the chemical structure of the N functional groups as well as the mechanism behind the chemical transformations in going from GO to the modified forms of GO.

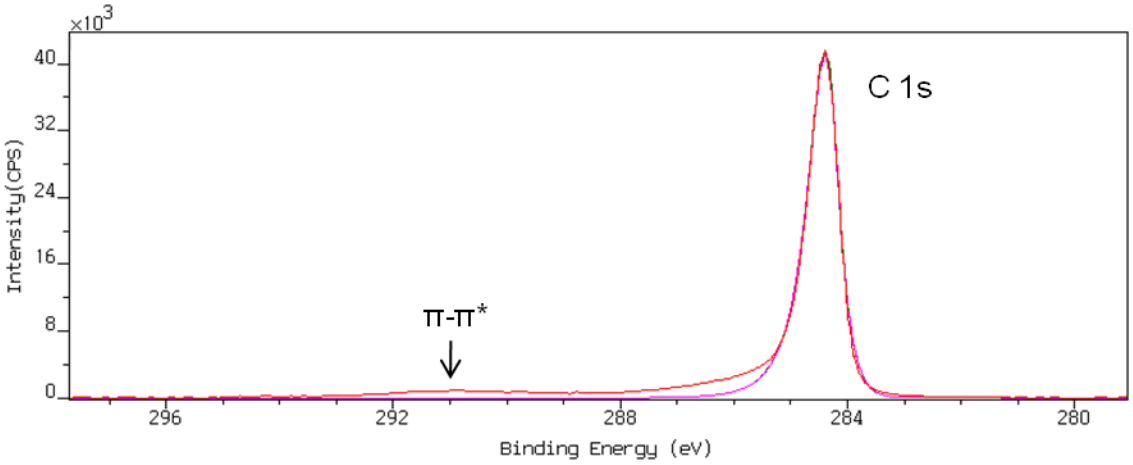

Figure 2-9. XPS high-resolution analysis of the C 1s region in graphene.

The XPS high resolution analysis of the C 1s region in graphene presents two peaks. A narrow peak centered at 284.4 eV corresponding to the C 1s peak and a broad peak around 291 eV corresponding to the π-π^* transition.

The narrow C 1s peak presents an asymmetric shape. Attekum and Wertheim reported similar results for HOPG.[62] Asymmetric peak shapes are typical of conductive materials. In graphite, peak asymmetry is explained by electron-hole pair formation that induces a screening of core electrons.[63, 64]

In addition to the source of peak asymmetry due to its conductive nature, the presence of oxygenated C atoms induces peak broadening towards higher energies. As reported above, the XPS survey spectrum of graphene shows a 4.6 atomic % content of O atoms. Estrade-Szwarckopf reported on the contribution of O functional groups to the high energy tail of the asymmetric peak in graphite samples where structural disorder was induced by different milling conditions.[65]

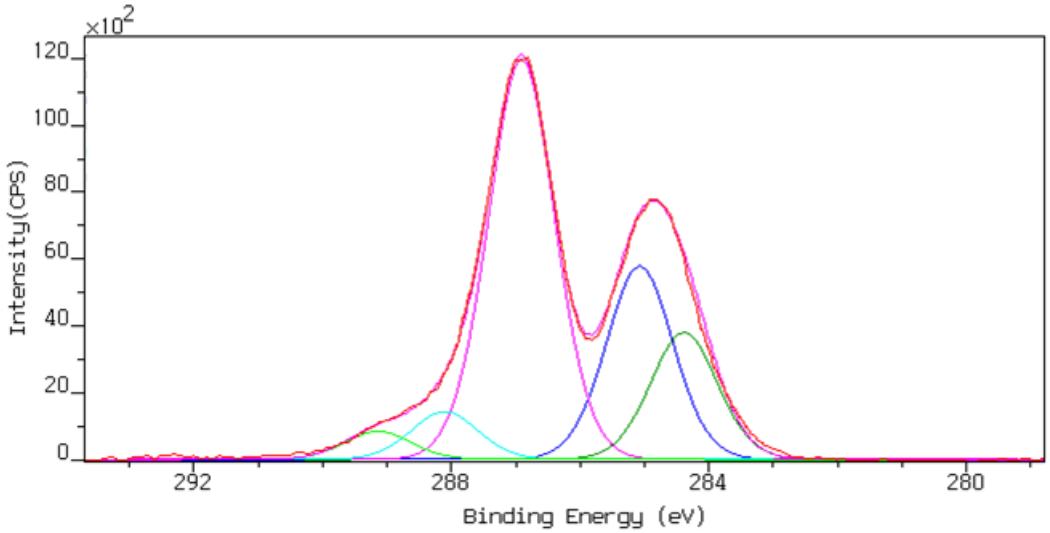

Figure 2-10. XPS high-resolution analysis of the C 1s region in GO.

Binding energy (eV)	Shift (eV)	FWHM	Atomic %	Carbon chemistry
284.4	(0.7)	1.2	16	Graphene
285.1	-	1.2	24.3	Saturated hydrocarbon
286.9	1.8	1.2	50.2	Hydroxyl & Epoxy
288.1	3	1.2	6	Carbonyl
289.2	4.1	1.2	3.5	Carboxylic

Table 2-6. Summary of the high-resolution XPS analysis in GO.

The XPS high resolution analysis of the C 1s region in GO shows a C 1s peak with two shoulders. A right-hand shoulder centered at lower binding energies between 284.5 and 285 eV, and a left-hand shoulder centered around 287 eV. The left-hand shoulder corresponds to functionalized C atoms and the right-hand shoulder to un-functionalized C atoms.

A total of 50.2 atomic % of the O functionalities in GO are hydroxyl or epoxy and a 3.5 atomic % corresponds to carboxylic acid groups. This observation is in good agreement with the pH of 2 measured on aqueous dispersions of GO. This analysis shows that 16 % of the C atoms in GO are in graphene regions. The remaining 84 % are oxidized C atoms and un-oxidized saturated hydrocarbons.

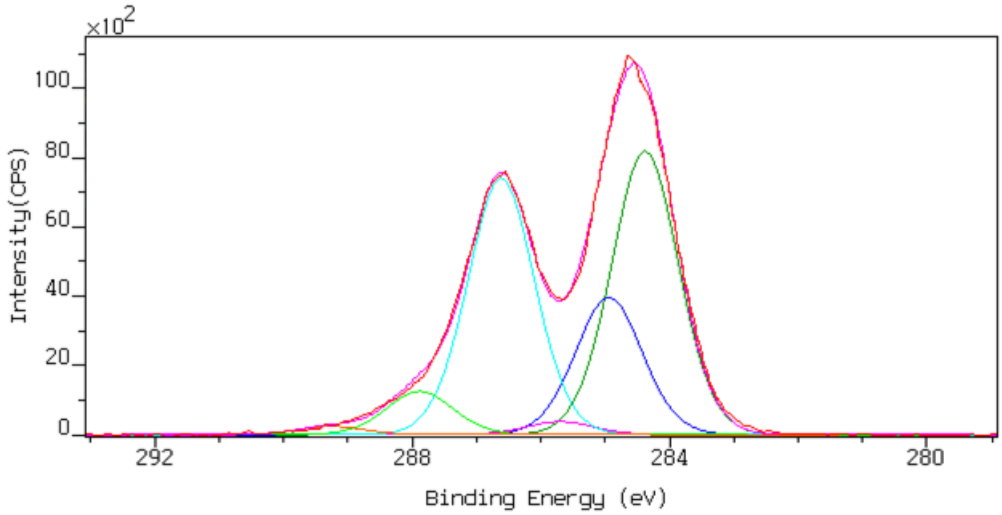

Figure 2-11. XPS high-resolution analysis of the C 1s region in MGO (foam).

Binding energy (eV)	Shift (eV)	FWHM	Atomic %	Carbon chemistry
284.4	(0.6)	1.2	38.2	Graphene
285	-	1.2	18.5	Saturated hydrocarbon
285.7	0.7	1.2	1.8	Nitrogen
286.6	1.6	1.2	34.5	Hydroxyl & Epoxy
287.9	2.9	1.2	5.8	Carbonyl
289.3	4.3	1.2	1.1	Carboxylic

Table 2-7. Summary of the high-resolution XPS analysis in MGO (foam).

In the high resolution XPS spectrum of MGO (foam) the intensities of the shoulders reverse with respect to GO. The increase in intensity of the right-hand shoulder comes primarily from its lowest energy component corresponding to C atoms in graphene regions. The right-hand shoulder corresponding to un-functionalized C atoms is now more intense than the left-hand shoulder corresponding to functionalized C atoms. This relative decrease in functionalized versus un-functionalized C atoms is due to a loss of O atoms and to an increase in graphene regions. The alkaline condition provided by IPDA reduces GO. The reduction of GO is shown in an increase in graphene content from 16 atomic % in GO to 38.2 atomic % in MGO (foam).

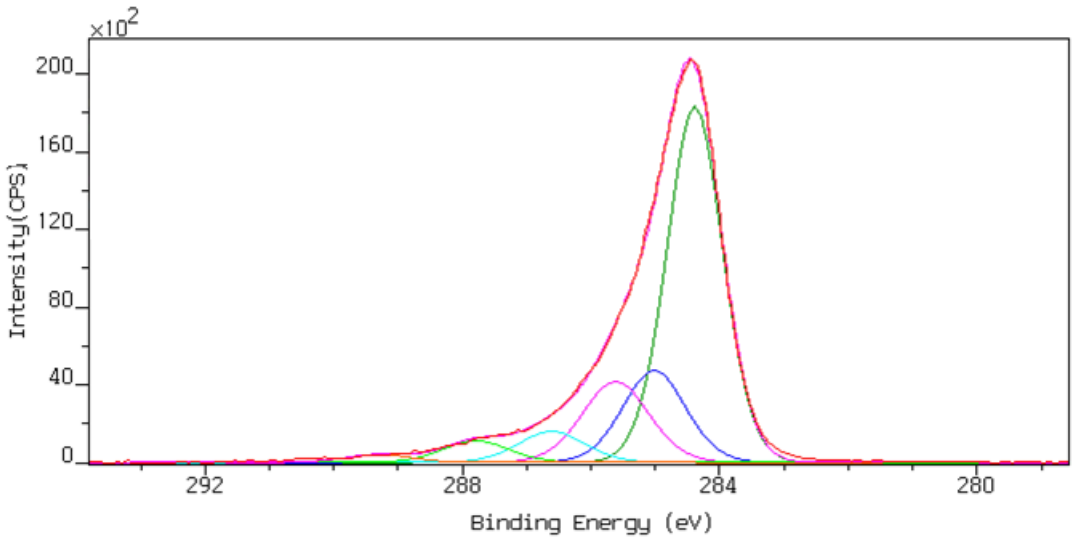

Figure 2-12. XPS high-resolution analysis of the C 1s region in MGO (nanocomposite).

Binding energy (eV)	Shift (eV)	FWHM	Atomic %	Carbon chemistry
284.4	(0.6)	1	56.6	Graphene
285	-	1.1	16.5	Saturated hydrocarbon
285.6	0.6	1.2	15.4	Nitrogen
286.6	1.6	1.2	5.9	Hydroxyl & Epoxy
287.8	2.8	1.2	4.1	Carbonyl
289.3	4.3	1.2	1.5	Carboxylic

Table 2-8. Summary of the high-resolution XPS analysis in MGO (nanocomposite).

The trends observed in the high-resolution XPS analysis of MGO (foam) are enhanced in MGO (nanocomposite). The heat provided to the sheets during the dehydration step results in further reduction and loss of O functionalities which reflects in a drop in the intensity of the left-hand shoulder and an increase in the intensity of the right-hand shoulder. The thermally induced reduction of the sheets results in an increase in graphene content up to 56.6 atomic %.

2.3.3. X-ray diffraction

XRD is used to analyze the thickness of the graphene sheets. Changes in thickness are monitored through changes in the interlayer spacing in crystallites made of stacks of sheets.

The interlayer spacing is the interplanar spacing between successive planes defined by the stacking of sheets. This is the one-dimensional period normal to the plane of the sheets. The interlayer spacing is determined from Bragg's condition

$$n\lambda = 2\,d\sin\theta$$

where n is an integer corresponding to the order of the reflection, λ is the wavelength of the x-rays, d is the interplanar spacing between successive crystallographic planes, and θ is the angle between the atomic plane and both the incident and reflected beams.

Graphite has a layered structure made of stacks of graphene sheets. The hexagonal form of graphite corresponds to an $(AB)_n$ stacking of sheets. Hexagonal graphite has the space group $P\,6_3/mmc$ (194) and the unit cell dimensions are a = 0.246 nm and c = 0.671 nm. The interlayer spacing (d_{002}) is 0.335 nm. This corresponds to a stacking of about 3 sheets per nm along the crystallographic c-axis which is the axis normal to the plane of the sheets.[66]

Table 2-9 summarizes the changes in interlayer spacing. The interlayer spacing increases from 0.34 nm in graphene to 0.79 nm in GO, to 1.14 nm in MGO (foam) and to 1.34

	Interlayer spacing (nm)	Crystallite size L_{00l} (nm)	Crystallite size Sheets (#)	Peak position (°2θ)	FWHM (°2θ)
Graphene	0.34			26.57	0.05
GO *sealed sample*	0.79	7	8.8	11.2	1.1
MGO (foam)	1.14	8.5	7.5	7.74	0.9
MGO (nanocomposite)	1.34	4.5	3.4	6.58	1.7

Table 2-9. Summary of the XRD analysis.

nm in MGO (nanocomposite). Interlayer spacings are calculated from the narrower peaks observed in the spectra at lower angles. These are the peaks centered at 26.57, 11.2, 7.74 and 6.58 °2θ in the graphene, GO, MGO (foam), and MGO (nanocomposite) spectra respectively in Figure 2-13. An increasing thickness of the sheets results in the (00l) peak shifting to lower angles.

The XRD spectrum of graphene shows that it is a highly crystalline form of graphite. The peak at 26.57 °2θ corresponds to the (002) reflection in hexagonal graphite with a measured interplanar spacing of 0.335 nm. This interlayer spacing matches the standard interlayer spacing obtained using SP-1 graphite which is a single-crystal form of flake graphite.[67]

The broad bumps in Figure 2-13-C and D are the result of a disordered aggregation of the sheets. This amorphization is attributed to a higher dispersion in sheet thickness which would reduce the ability of the sheets to form periodic stacks with long range order.

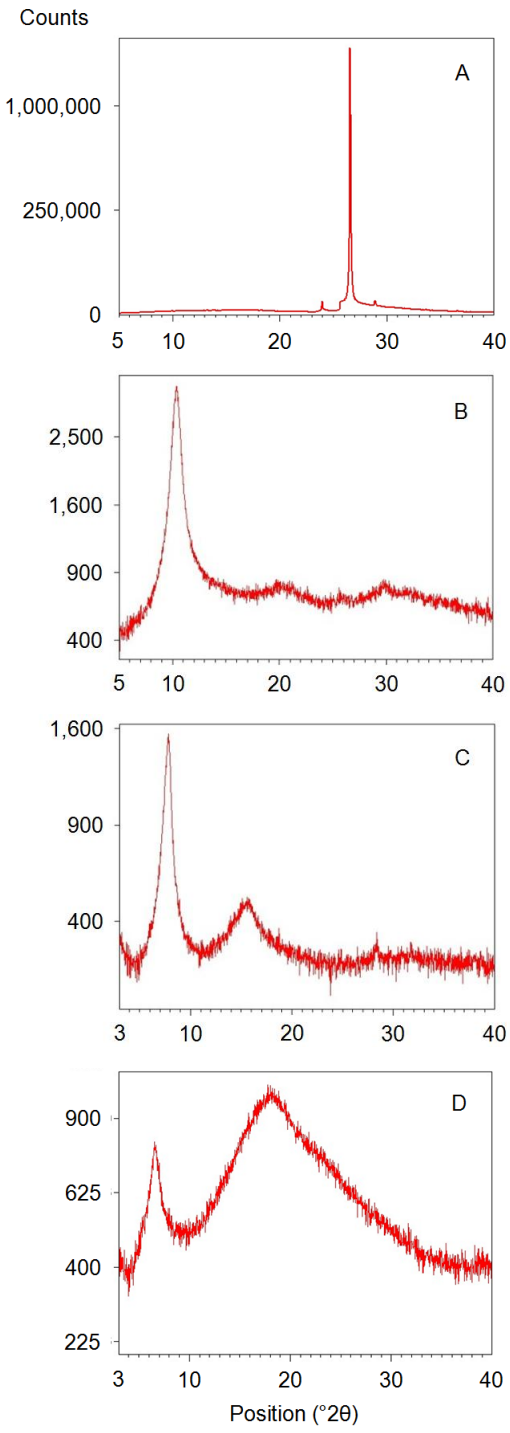

Figure 2-13. XRD spectra of (A) graphene, (B) GO, (C) MGO (foam), and (D) MGO (nanocomposite). Note the position scale changes from 5-40 in (A) and (B) to 3-40 in (C) and (D) in order to capture the entire peak base.

XRD analysis of GO shows the disappearance of the 0.34 nm interlayer spacing of graphite jointly with the appearance of a new broader diffraction peak at lower angles corresponding to an interlayer spacing of 0.79 nm. The bonding of oxygenated functional groups to C atoms in the sheets causes this increase in interlayer spacing. XPS analysis shows an increase in N content as GO is treated with IPDA and further after dehydration at 200 °C in the presence of IPDA. XRD shows an increase in interlayer spacing which is attributed to an increase in sheet thickness due to the incorporation of IPDA molecules.

The dispersion in sheet thickness would reduce the ability of the sheets to pack into periodic stacks since this requires layers of similar thickness. The thickness of the crystallites made of stacks of sheets can be estimated from the breadth of the (00l) peak. A higher dispersion in thickness would result in smaller crystallite size which would cause broadening of the (00l) peak. Peak broadening can arise from small crystallite size and/or lattice distortion among other factors. In the present analysis, peak broadening is assumed to come entirely from the contribution due to the small size of the crystallites.[68]

The relation between crystallite size and the breath of the peak is captured in Scherrer's equation

$$L_{00l} = \frac{K\lambda}{\beta \cos\theta}$$

where L_{00l} is the crystallite size, K is a constant that depends on the shape of the crystallites, λ is the wavelength of the x-rays, β is the full width at half-maximum of the 00l reflection and θ

is the peak position. The constant K is 0.89 for crystals with a platelet shape. In this analysis, the measured crystallite size corresponds to the thickness of the stack of sheets along the normal to the plane of the sheets.

In GO, the thickness of the crystallites is 7 nm. This corresponds to a stacking of 8.8 sheets. In MGO (foam), the thickness of the crystallites is 8.5 nm. This thickness is higher than in GO crystallites but corresponds to a stacking of 7.5 sheets. This is a lower number of sheets compared to the GO crystallites where the sheets are thinner. In MGO (nanocomposite), the thickness of the crystallites is 4.5 nm which corresponds to 3.4 sheets per crystallite.

In addition to the decrease in crystallite size, the increasing relative intensity of the amorphous bump with respect to the (00l) peak further supports a higher dispersion in sheet thickness in MGO (nanocomposite) compared to MGO (foam). As shown later in the TEM analysis, a coating seems to gradually build up on the sheets during processing. This coating increases the roughness of the sheets and may contribute to sheet thickness dispersion.

Graphite oxide is a hygroscopic material. Buchsteiner et al. showed that the interlayer spacing in graphite oxide varies with its degree of hydration. Interlayer spacing in graphite oxide changes reversibly from 0.6 to 1.2 nm with increasing relative humidity.[69]

The interlayer spacing of GO reported in Table 2-9 corresponds to the analysis carried out on a sealed sample in order to prevent uptake of ambient moisture. When the analysis is

conducted without sealing the sample, the interlayer spacing increases from 0.79 nm to 0.85 nm.

When sealed and unsealed measurements are carried on the modified forms of GO, the following interlayer spacing are observed. MGO (foam): sealed 1.14 nm, unsealed 1.14 nm and MGO (nanocomposite): sealed 1.37 nm, unsealed 1.34 nm. The absence of interlayer spacing increase when measurements are conducted unsealed indicates that the modified forms of GO are less prone to uptake ambient moisture than GO. The absence of water uptake is attributed to changes in the surface chemistry of the sheets from hydrophilic in GO to more hydrophobic in the modified forms of GO.

2.3.4. Transmission electron microscopy

The motivation for TEM analysis was to determine the presence of graphene regions in GO and in the modified forms of GO in order to support the XPS energy referencing strategy.

As explained above, GO sheets can contain un-oxidized regions. Wilson et al. showed that the same hexagonal spot diffraction pattern found in graphene can be observed in GO. The presence of single-crystal diffraction patterns in GO shows that the graphene regions have the same a-axis orientation which indicates that they are un-oxidized regions of the original graphene sheets.[70]

TEM diffraction analysis of GO and the modified forms of GO demonstrates that all the sheets contain graphene regions. Figure 2-14 shows the characteristic hexagonal single-crystal diffraction pattern of graphene in GO. The intensity profile along the dashed line is reported in Figure 2-15. The ratio of intensities corresponding to the ratio of the peak maxima is $I_{-1010} / I_{-2110} = 1.8$. This ratio of relative intensities corresponds to an inversion with respect to the relative intensities in graphite. This is due to a lack of AB-type of periodicity in the stacking of layers. This can occur when the sample is a monolayer sheet or if there is no AB-type of crystallographic registry between graphene regions from adjacent sheets in multilayer stacks of sheets. The same reverse order of relative intensities is observed in GO and in the modified forms of GO in films made of multiple stacks of sheets as shown in Figures 2-16 to 2-18.

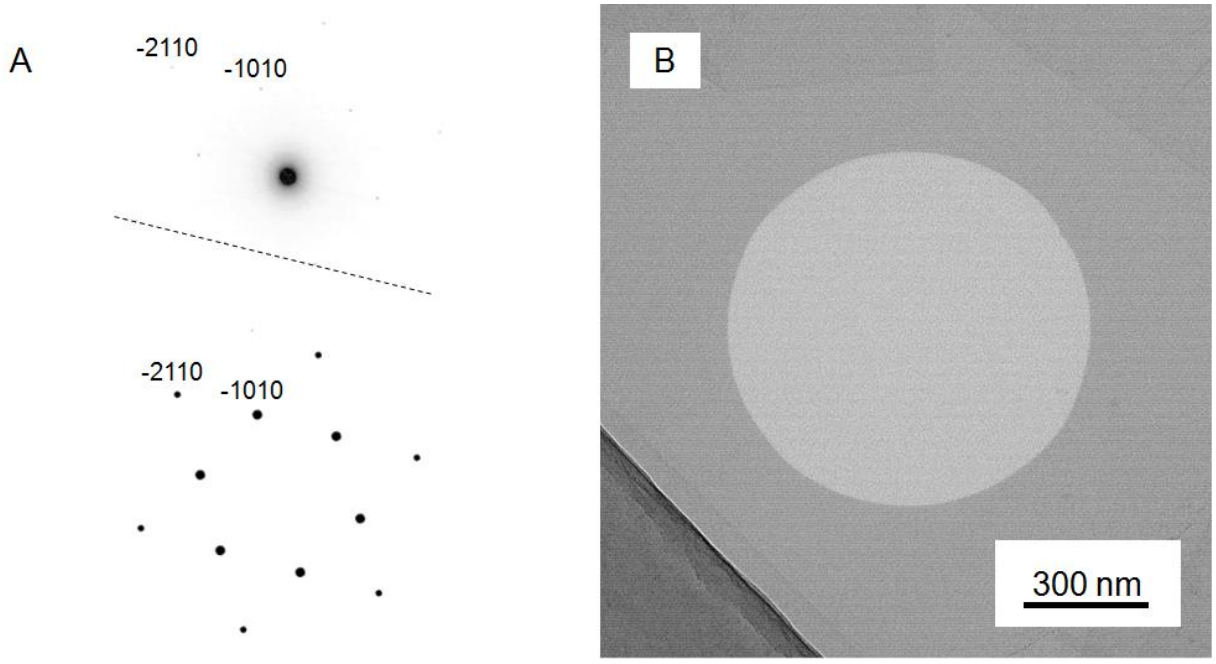

Figure 2-14. TEM diffraction analysis of GO. (A) TEM selected area diffraction pattern. The single-crystal diffraction pattern indicates that the graphene regions in GO share a common a-axis orientation. (B) TEM bright-field imaging highlighting the area selected in the diffraction analysis.

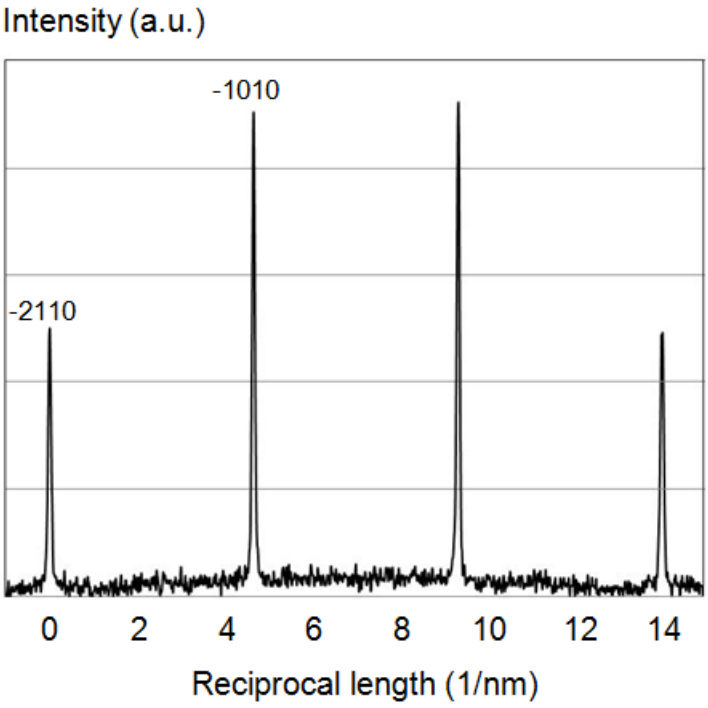

Figure 2-15. Intensity profile along the dashed line in Figure 2-14.

A coating on the sheets is visible in MGO (nanocomposite) as shown in Figure 2-18. This coating is attributed to the reaction of the sheets with IPDA. The coating results in a roughening of the surface of the sheets. This causes the dispersion in sheet thickness that reduces the ability of the sheets to crystallize as discussed during the XRD analysis.

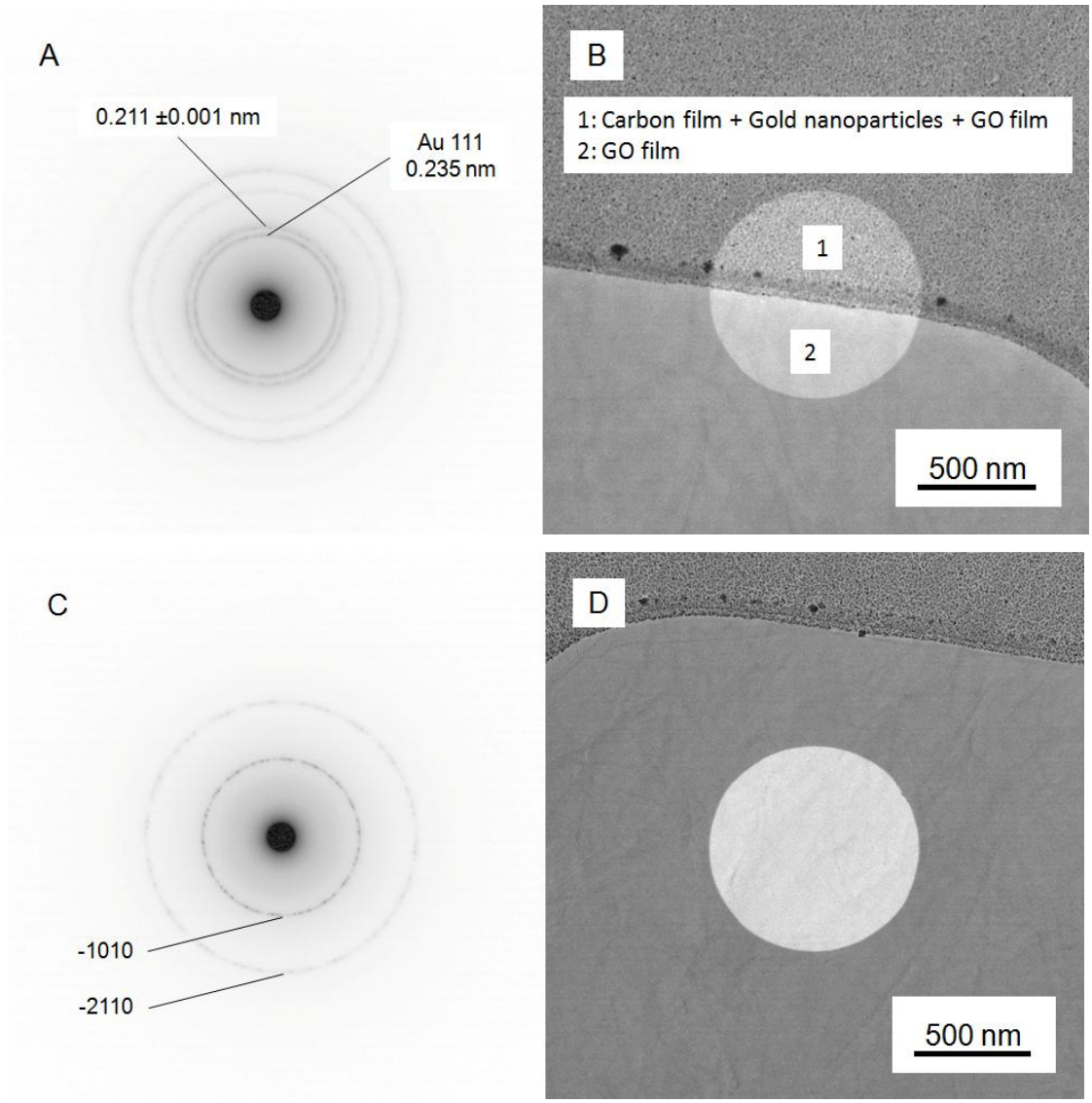

Figure 2-16. TEM diffraction analysis of a GO film. (A) Selected area composite diffraction pattern of GO and gold (Au) nanoparticles. The rings from the Au nanoparticles enable to calibrate the diffraction pattern.[71] The innermost reflection in GO corresponds to a d-spacing of 0.211 ±0.001 nm. This interplanar spacing is close to the 0.213 nm observed by Meyer et al. in mechanically cleaved graphene sheets corresponding to the -1010 planes.[72] (B) TEM bright-field image highlighting the area selected in the diffraction analysis in A. (C and D) TEM diffraction analysis and selected area image respectively of the GO film only.

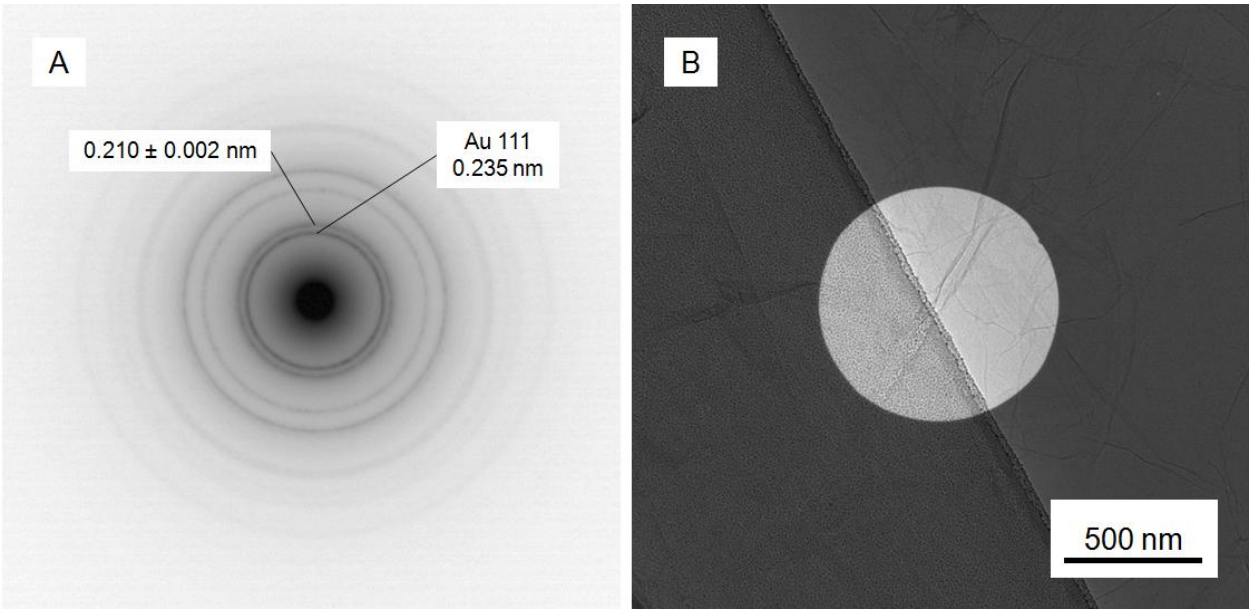

Figure 2-17. TEM diffraction analysis of a MGO (foam) film. (A) Selected area composite diffraction pattern of MGO (foam) and Au nanoparticles. (B) TEM bright-field image highlighting the area selected in the diffraction analysis.

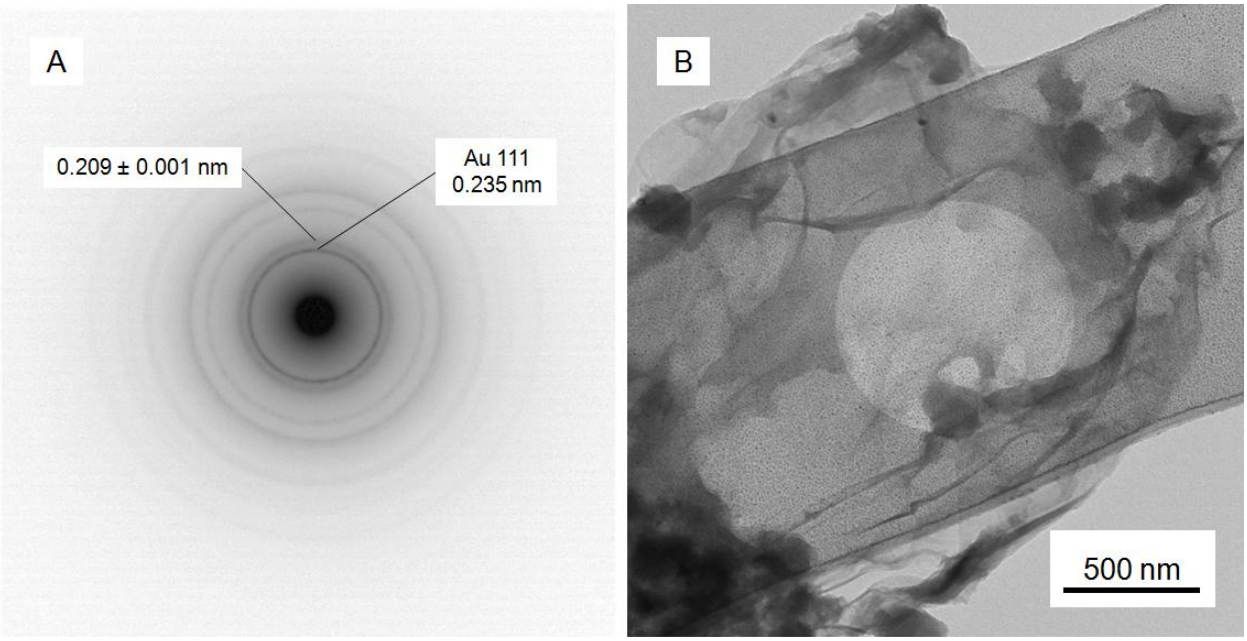

Figure 2-18. TEM diffraction analysis of a MGO (nanocomposite) film. (A) Selected area composite diffraction pattern of MGO (nanocomposite) and Au nanoparticles. (B) TEM bright-field image of the area selected in the diffraction analysis.

Chapter 3

Liquid foams of graphene

This chapter is organized into 4 sections. The first section gives an introduction to liquid foams. The second section reports the structural analysis of the LFG. The third section proposes a mechanism to explain the formation and stability of the LFG. The fourth section reports the analysis of the mechanical properties of the graphene shells.

3.1. Introduction

Liquid foams are dispersions of bubbles in a liquid. Bubbles are stabilized by foaming agents that position at the interface between the gas and the liquid.[73] Weaire and Hutzler differentiate between two liquid foam regimes: dry foams, where bubbles take form of polyhedral cells with little liquid in between, and wet foams, where liquid increases swelling the Plateau borders. In the limit of wet foams, bubbles recover a spherical shape.[74]

To make aqueous foams, typical surfactants are amphiphilic molecules made of hydrophilic and hydrophobic parts combined into linear or branched chain molecular structures. Surfactants are classified according to the type of hydrophilic group as anionic, cationic, amphoteric and nonionic. The hydrophobic segment is typically a hydrocarbon chain. The hydrocarbon segment may include alkyl groups forming a linear chain, alkyl groups forming a branched chain, unsaturated alkenyl chains, alkylbenzenes or alkylnaphtalenes to mention a few. Other so called specialty surfactants contain fluorinated or silicone based chains as hydrophobic segments.[75] The common sodium dodecylsulfate is an anionic surfactant where the sulfate group provides the hydrophilic character and the dodecyl chain the hydrophobic character. The structure of liquid foams made with sodium dodecylsulfate is shown in Figure 3-1. The adsorption of surfactant molecules at the gas-liquid interface reduces the surface tension of the bubbles and stabilizes them. The hydrophilic part of the sodium dodecylsulfate molecule is in contact with water, in the liquid, and the hydrophobic part is inside the bubble, in the gas.[76]

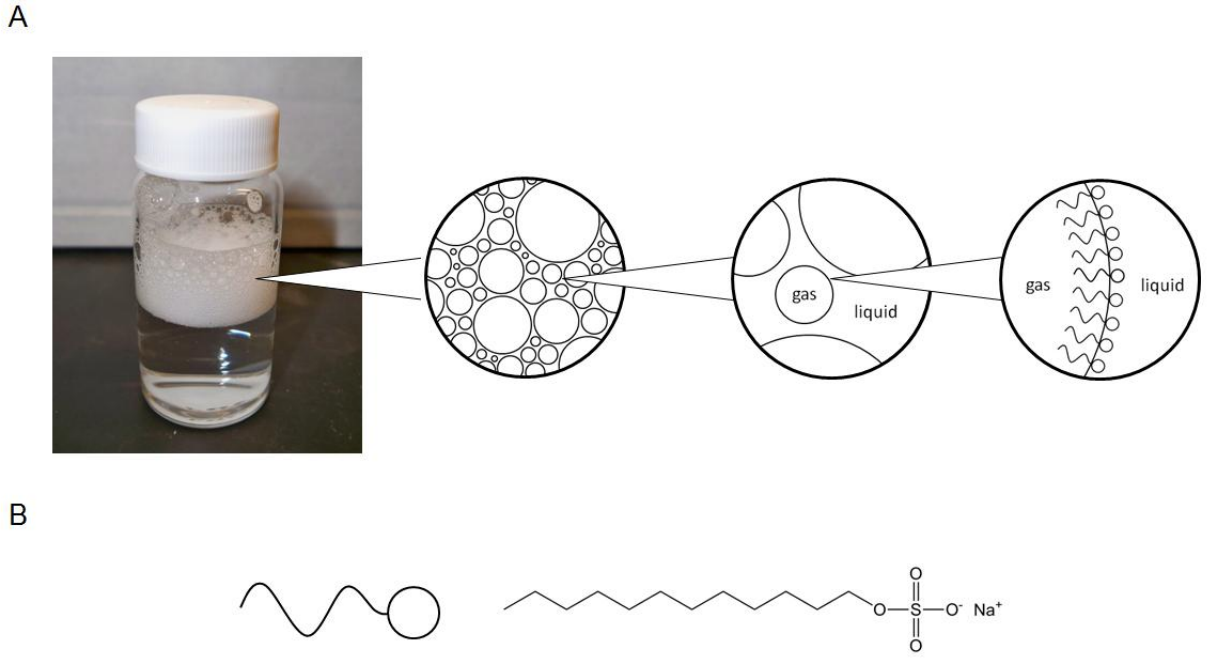

Figure 3-1. Liquid foam made with sodium dodecylsulfate. (A) Schematic of the hierarchical structure of the foam. Air bubbles are stabilized by sodium dodecylsulfate molecules that position at the gas-liquid interface. (B) Chemical structure of sodium dodecylsulfate.

3.2. Structure of the foams

LFG form upon agitating aqueous mixtures containing IPDA modified GO (IPDA-GO). IPDA-GO is labeled MGO (foam) in the previous chapter. The structure of LFG is summarized in Figures 3-2 and 3-3. Air bubbles are encapsulated inside graphene shells made of IPDA-GO sheets. Cilia-like filaments are seen protruding from the shell surface. These protrusions are attributed to folds in the sheets or to edge-segments of the sheets. Upon encapsulation of the air bubbles, the gas-liquid interface is substituted by a combination of two interfaces, a gas-shell and a shell-liquid interface.

The preparation of the LFG is reported in the previous chapter together with the analysis of the IPDA-GO sheets. This section analyzes the bubbles in their wet state as found in the LFG as well as in their state out of the liquid as dried graphene shells.

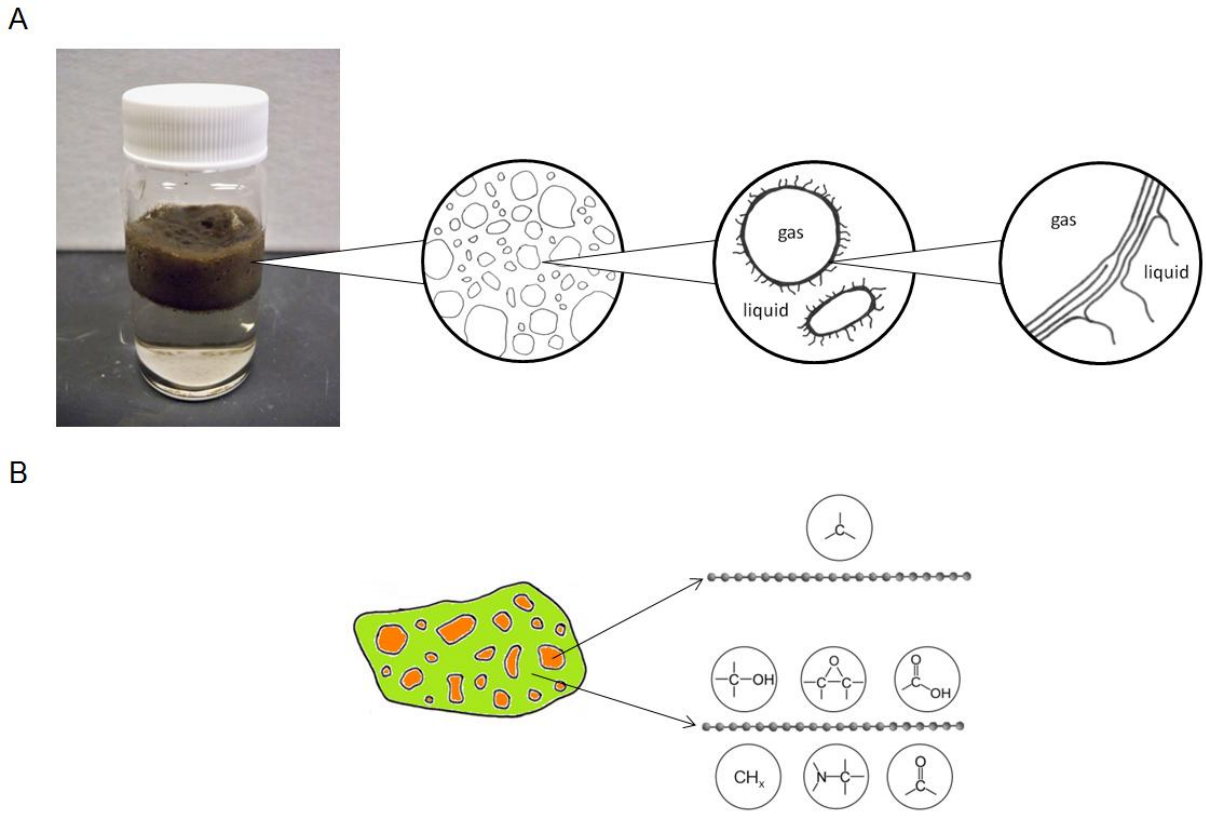

Figure 3-2. Liquid foam made with IPDA-GO. (A) Schematic of the hierarchical structure of the foam. Air bubbles are encapsulated inside graphene shells. (B) Chemical structure of IPDA-GO. Left, view normal to the plane of the sheet illustrating the heterogeneous distribution of graphene regions and functionalized graphene regions. Right, edge-on view of the sheet indicating the types of C chemistries present in each one of the regions.

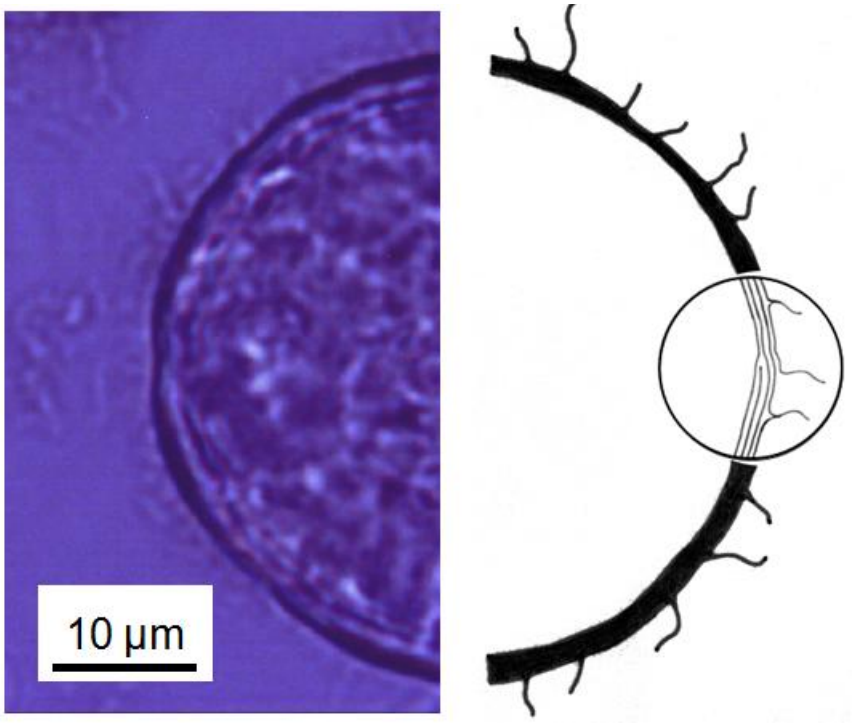

Figure 3-3. Structure of the bubbles in the LFG. Left, transmission light microscope image of a bubble suspended in the liquid. Right, schematic of the cross-section of the graphene shell. The shell has a concentric layered structure made of IPDA-GO sheets forming a few nanometers thick barrier impermeable to air. The cilia-like filaments on the shell surface are attributed to folds in the sheets or to edge-segments of the sheets. Sample preparation consisted in sandwiching an aliquot of the foam between glass slides.

In LFG bubbles present a distribution of shapes and sizes. Most bubbles have spherical and ellipsoidal shapes as shown in Figure 3-4. The distribution of bubbles sizes is shown in the histogram in Figure 3-5. Over a population of 100 bubbles, sizes ranged from 4 µm to 164 µm with an average size of 55 µm. The size of the bubbles should at least depend on factors such as the size of the graphene sheets and the size of the air bubbles generated during the foaming process. The possibility to tune these parameters offers a basis for foam engineering.

Spreading the foam between two glass slides allows the study of individual bubbles. On heating, the thermal expansion of the encapsulated air causes the deformation of the shell. As the thermal expansion continues, the shell eventually ruptures releasing the air as shown in the sequence of images in Figure 3-6.

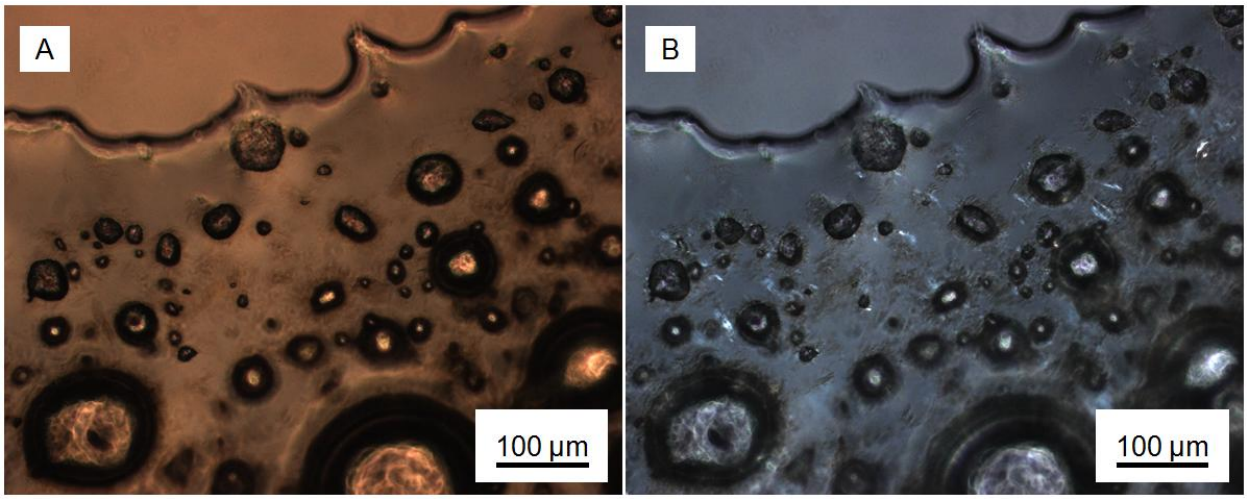

Figure 3-4. Dispersion of bubbles in a drop of LFG. (A) Transmission light microscope image of a drop of the foam deposited on a glass slide. (B) Imaging conducted between crossed-polars. The analysis corresponds to the edge of the drop where the bubbles are more spread out. The featureless region on top of the image is the glass support. Sample preparation consisted in depositing an aliquot of the foam on a glass slide.

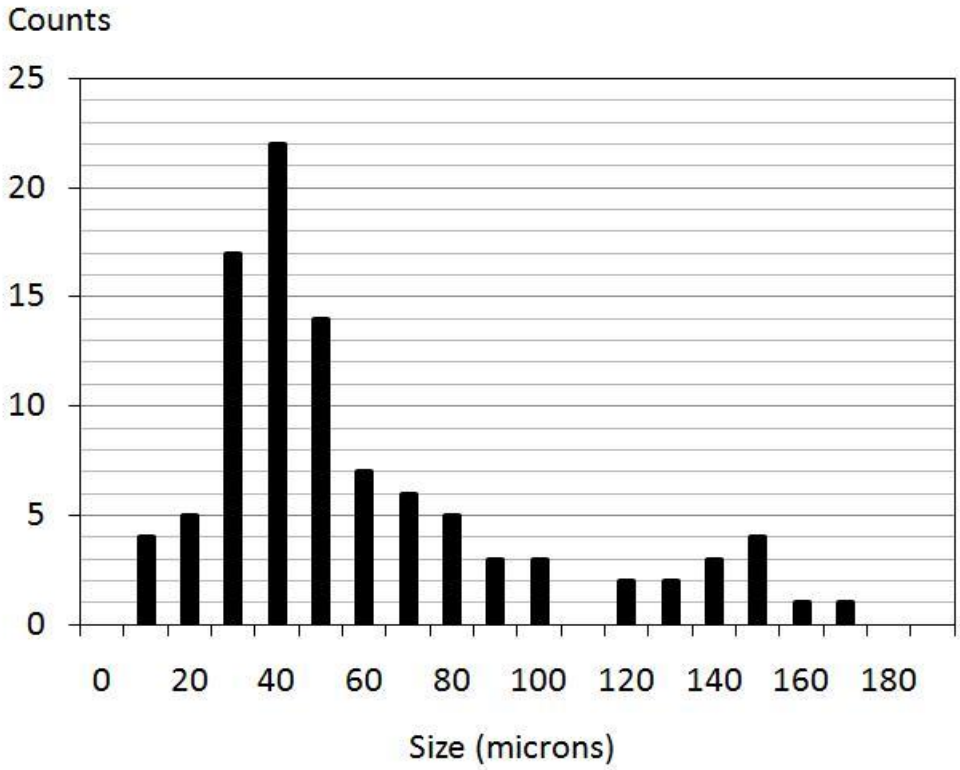

Figure. 3-5. Distribution of bubbles sizes. Sizes correspond to the average of the shortest and longest dimensions of each bubble. The average bubble size is 55 μm.

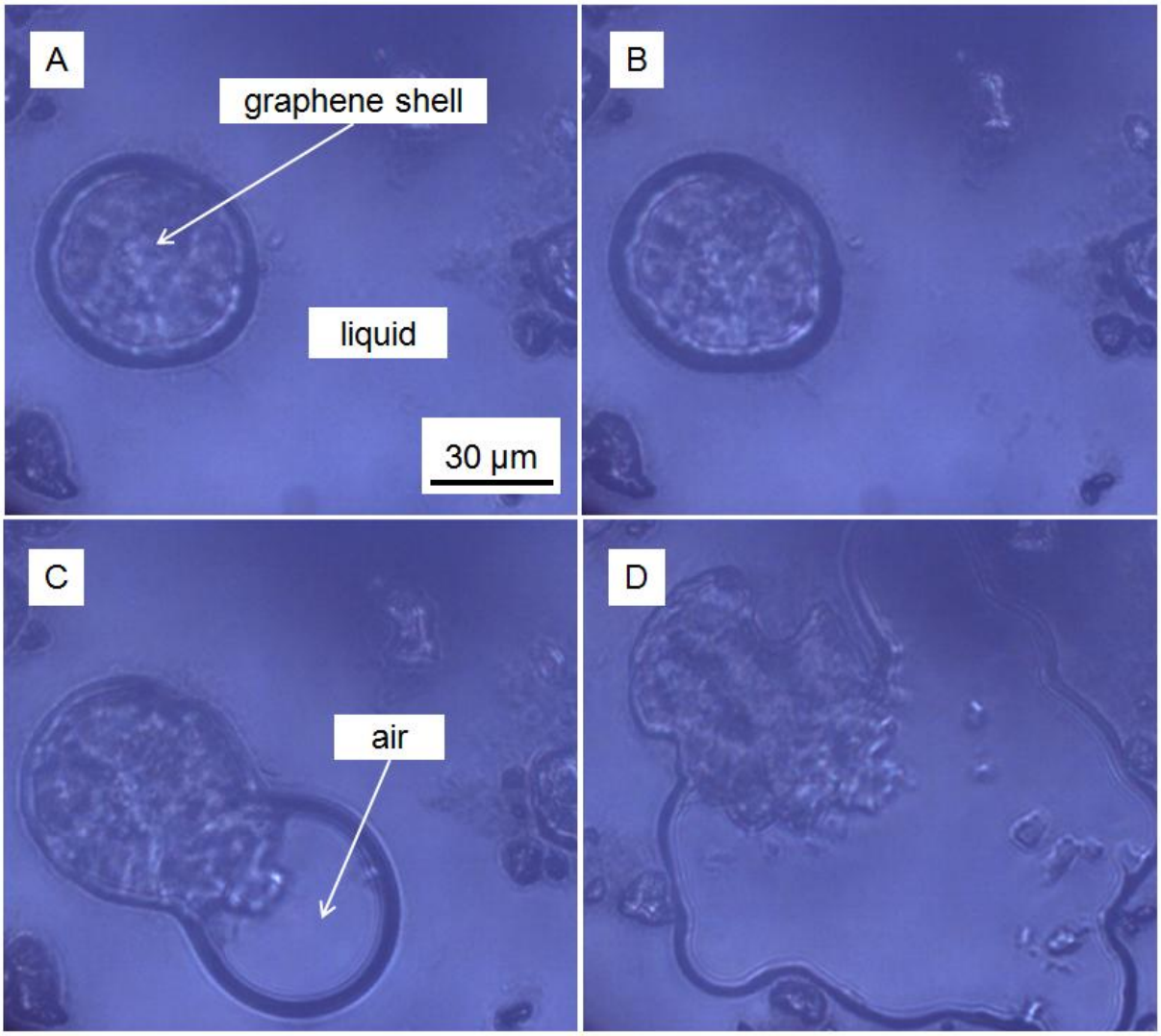

Figure 3-6. Thermal expansion and burst of a bubble. The graphene shell deforms and then bursts as a result of the increase in internal air pressure. The blurring of the shell contour due to optical aberration enables visualization of the changes in the thickness of the bubble during the air release process. Upon releasing the air, the dark line becomes thinner indicative of the collapse of the shell.

Figure 3-7 shows an SEM image of a cluster of dried graphene shells. The absence of charging during SEM imaging indicates that the graphene shells are conductive enough to avoid electric charge buildup. This demonstrates the recovery towards graphene electrical properties in IPDA-GO.

A distribution in the barrier properties of the shells is expected since each one of the IPDA-GO sheets has a different chemical structure, size and shape; factors that may contribute to gas encapsulation efficiency. Hence, shells with good barrier properties may retain the gas longer and under vacuum conditions, whereas shells with poor barrier properties may more easily release the gas and collapse.

The outer surface of the dried shells is wrinkled. Figure 3-8 is an SEM image of the shell surface. The wrinkles appear brighter in the SEM due to higher emission of secondary electrons as a result of their higher surface per probing area. The wrinkles are folds in the IPDA-GO sheets. The sheets are not wrinkled before wrapping the air bubbles as shown in the TEM analysis in Figure 2-17.

IPDA-GO is a flexible molecular sheet where folding generates a fold line in the form of a molecular ridge.[77] The folding mechanism in molecular sheets should be similar to the mechanism proposed by Storks to explain folding in molecular chains of polymers. This is folding by a mechanism of rotation around C bonds.[78]

A wrinkled shell surface is probably present in the wet as it is observed in the dried state. The protruding filaments coming out of the wet shell surface in Figure 3-3 are attributed to folded regions or edge-segments of sheets. This is illustrated in the magnified section of the shell schematic in Figure 3-3 depicting two folds and one edge-segment in between the folds.

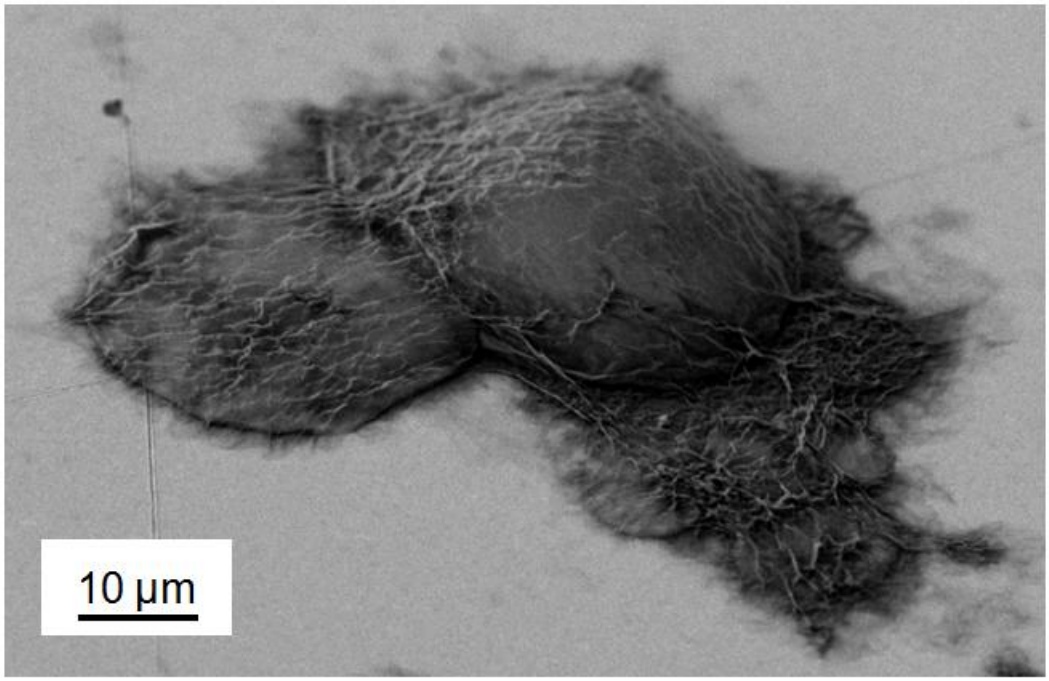

Figure 3-7. SEM image of a cluster of graphene shells. Apparently, the shell with the dome-like shape retains the encapsulated air while the other shells clearly released the air and collapsed. If the dome-shaped shell is actually retaining the air this would indicate that the barrier properties of the graphene shells can retain air under vacuum (SEM chamber ~10^{-4} Pa). A thin layer of IPDA-GO sheets is observed flat on the substrate around the shells. This feature is easier to visualize in the TEM image in Figure 3-11. Sample preparation: Aliquots of the foam were deposited on gold coated glass slides. Then samples were dried in a dessicator under a vacuum of 10 Pa during 24 h.

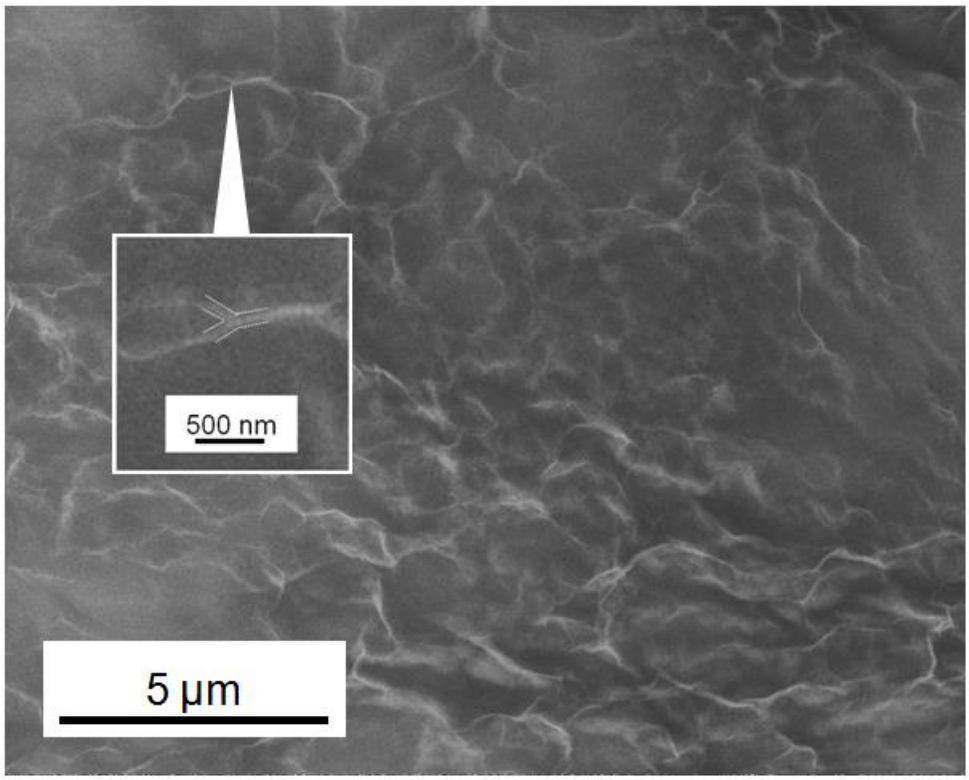

Figure 3-8. High-resolution SEM imaging of the wrinkles on the outer surface of a graphene shell. The wrinkles are folds in the IPDA-GO sheets. The magnified section highlights a bifurcation in a fold line. This is a typical feature found in flexible sheets, for example in fabrics. Sample preparation: Aliquots of the foam were deposited on gold coated glass slides. Then samples were dried in a dessicator under a vacuum of 10 Pa during 24 h.

In order to analyze the internal structure and the inner surface of the graphene shells, a shell is cut by means of focused ion beam (FIB) milling. The cut exposes the interior of the shell as shown in Figure 3-9. However, the use of FIB milling generates some artifacts due to the re-deposition of the milled substrate on the shell.

Fracturing the shells in liquid nitrogen affords a cleaner analysis and enables to study the internal structure of the shells. The fracture surface of a freeze-fractured cluster of shells is shown in Figure 3-10. This experiment enables imaging the internal structure and inner surface of the shells and measuring the thickness of the shells. The packing of IPDA-GO sheets in the shells has a layered structure. In Figure 3-10, shells are about 5 nm thick which corresponds to a stack of about 4 to 5 sheets.

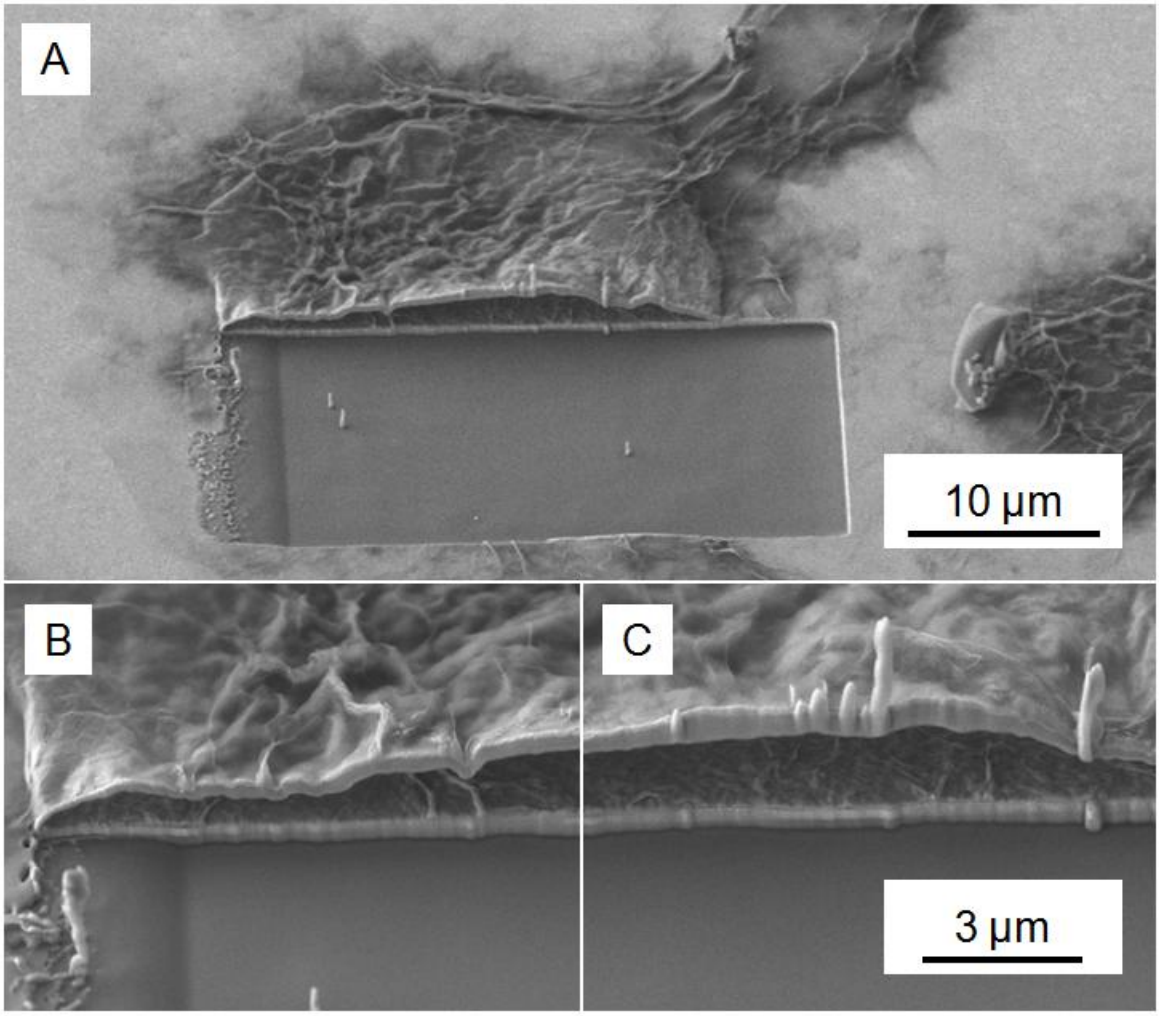

Figure 3-9. SEM image of a FIB milled graphene shell. The rectangular terrace in front of the cut corresponds to the area removed with the gallium ion beam. Re-deposition of the material milled from the substrate generates a coating increasing the thickness of the shell. Other artifacts produced by the same re-deposition mechanism are the columns looking like stalagmites. Sample preparation for FIB consisted in depositing an aliquot of the foam on a gold coated glass slide. Then the sample was dried in a dessicator under a vacuum of 10 Pa during 24 h. After FIB milling, the sample was imaged without further modifications.

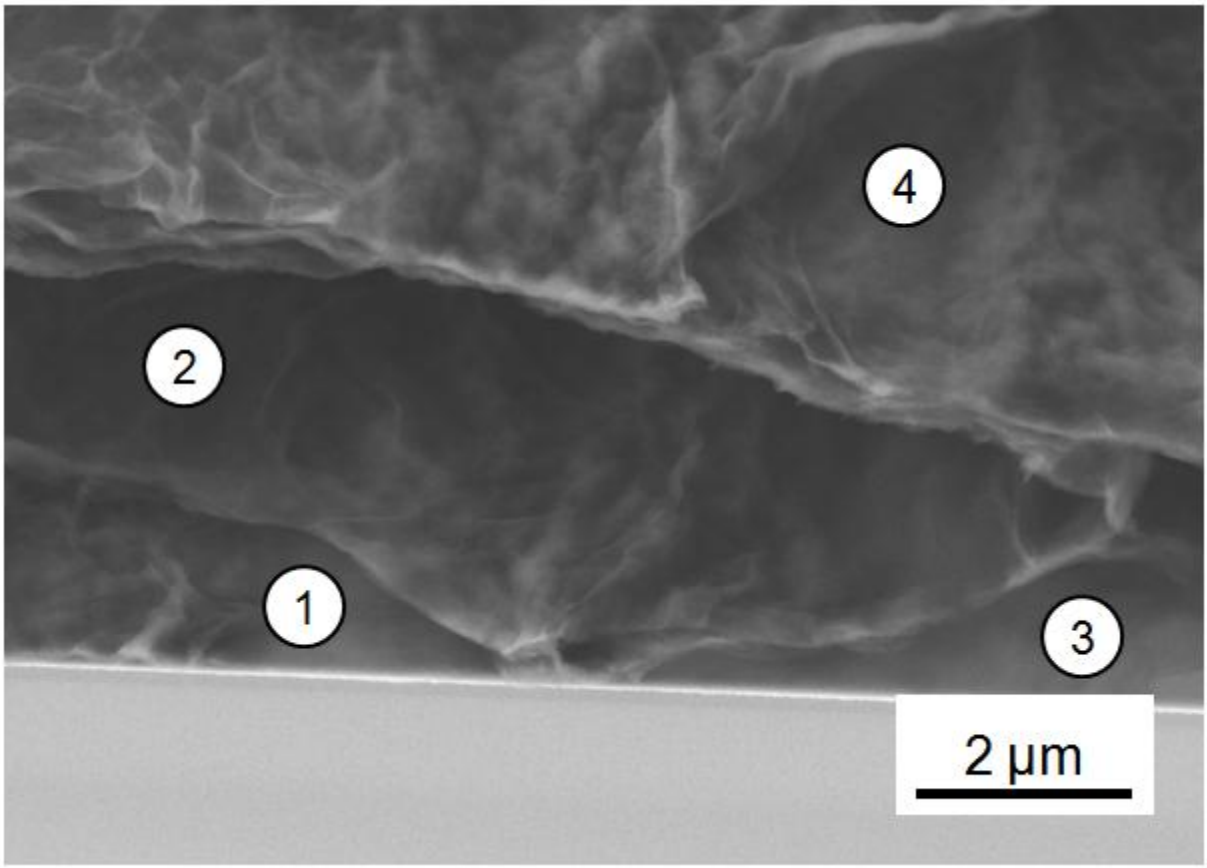

Figure 3-10. SEM image of the surface fracture of a freeze-fractured cluster of graphene shells showing the interiors of 4 shells. The clean fracture of the shells at the liquid nitrogen temperature shows the layered internal structure of the shells. Sample preparation consisted in depositing an aliquot of the foam on a gold coated silicon support, further drying the sample in a dessicator during 24 h and finally the sample was introduced in liquid nitrogen and fractured. The fracture bisected some of the graphene shells.

A TEM image of a graphene shell is shown in Figure 3-11. The TEM analysis shows edge-segments of the shell-forming sheets that come out of the shell to deposit flat on the carbon film support. These edge-segments are thought to be the cause of the larger filaments protruding from the shells surfaces in Figure 3-3.

The shells present a crystallinity coming from the graphene regions in the IPDA-GO sheets. These graphene regions are randomly oriented in the shell resulting in polycrystalline ring diffraction patterns when the entire shell is analyzed as shown in Figure 3-12. When a single area of one of the shell-forming sheets is analyzed, the pattern observed corresponds to the single-crystal diffraction of graphene as shown in Figure 3-13.

In the LFG, IPDA-GO is the foaming agent. The next section proposes a mechanism to explain the formation and stability of the foams.

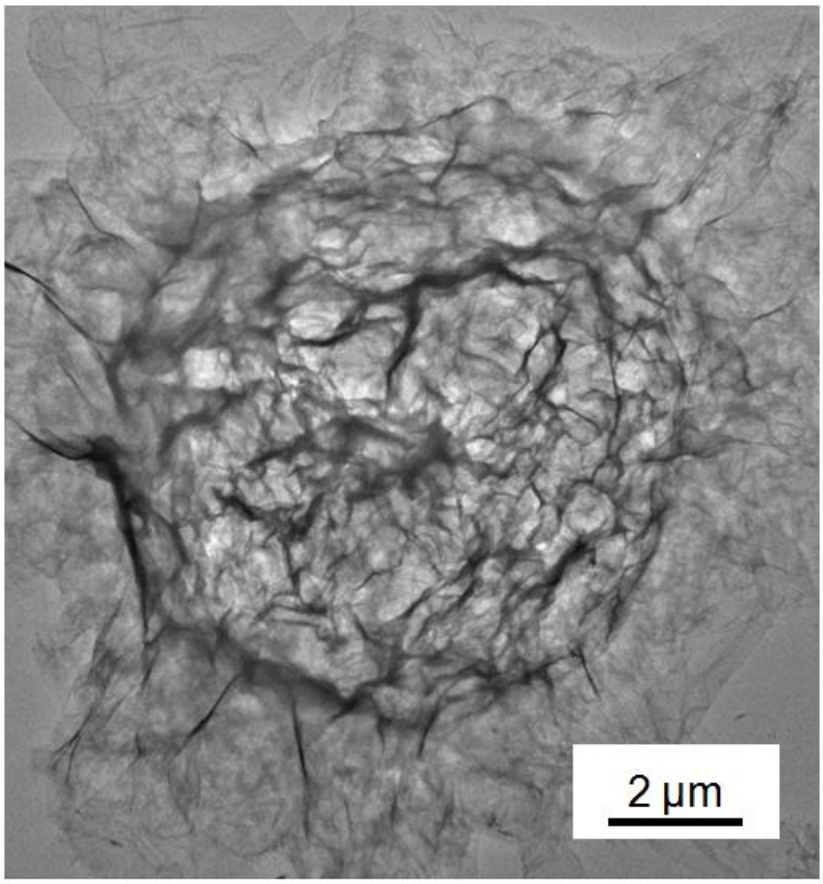

Figure 3-11. Bright-field TEM image of a graphene shell. Edge-segments of the shell-forming sheets are flat on the carbon film support around the shell. A magnified image of the edge-segment on the top-left region is shown in Figure 3-13.

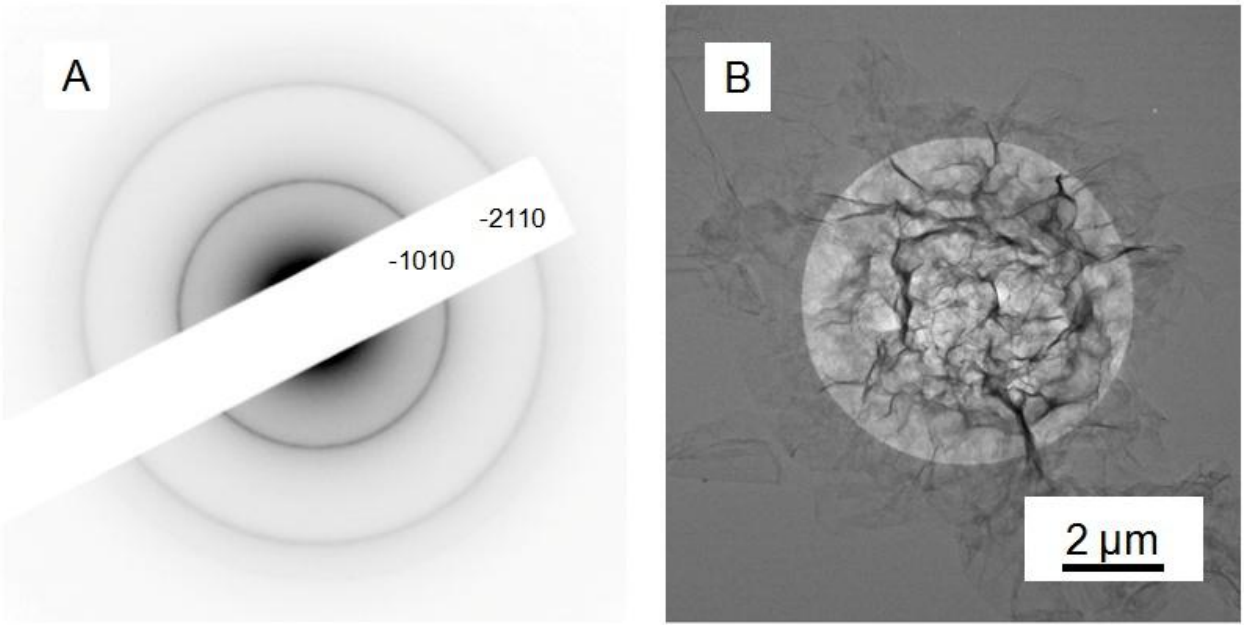

Figure 3-12. TEM diffraction analysis of a graphene shell. (A) The powder-like diffraction pattern is the result of the random distribution of graphene regions in the shell. (B) Bright-field TEM image highlighting the area selected in the diffraction analysis.

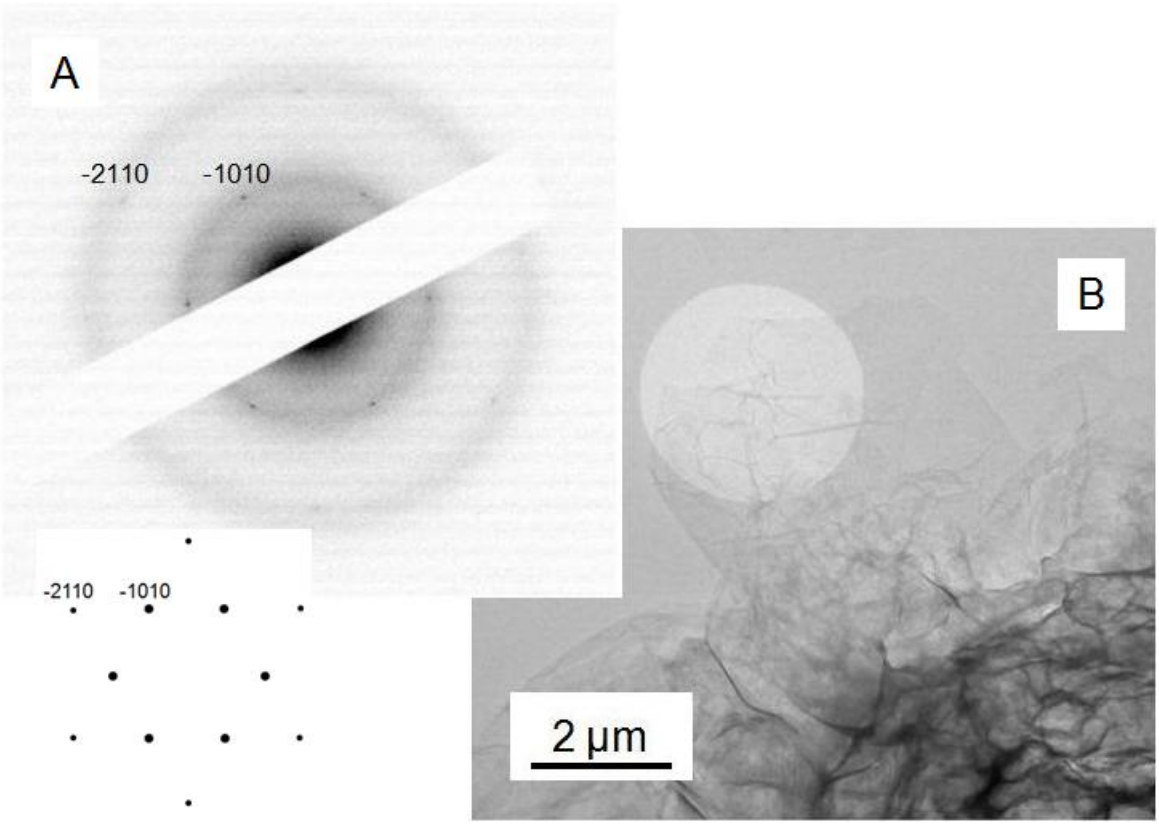

Figure 3-13. TEM diffraction analysis of an edge-segment of a shell-forming sheet. (A) Single-crystal diffraction pattern from the graphene regions in the sheet. The pattern observed is the hexagonal single-crystal diffraction pattern of graphene. The diffuse rings come from the amorphous carbon film support. (B) Bright-field TEM image highlighting the area selected in the diffraction analysis.

3.3. Graphene foaming mechanism

The formation of the LFG requires the IPDA-GO sheets to wrap the air bubbles. Figure 3-14 illustrates the proposed wrapping mechanism. The sheets are flexible enough to conform to the interface of the air bubble. In addition, the barrier properties of the sheets enable retention of the encapsulated air. It is suggested that the molecular forces driving the wrapping mechanism are hydrophobic in nature. It has been shown earlier that the IPDA modification of GO increases the hydrophobicity of the sheets. This increased hydrophobicity would explain the affinity of the sheets towards the air bubble interface which would then trigger the wrapping mechanism. After wrapping the air bubbles, buoyancy moves the shell encapsulated bubbles towards the liquid surface generating the foam. Foams are stable during at least 5 hours as shown in Figure 3-15. The stability of the LFG requires that the shelled bubbles do not completely phase separate from the liquid.

IPDA-GO presents two chemically distinct regions, the graphene regions and the functionalized graphene regions. Although IPDA-GO behaves as a hydrophobic material, for example regarding contact angle measurements or water uptake, the presence of both types of graphene regions makes the sheets amphiphilic. The hydrophobic graphene regions result in affinity for the air-liquid interface, enabling the formation of the shells around the air bubbles, and the functionalized graphene regions give the sheets enough affinity towards water to avoid the complete phase separation between the graphene shells and the liquid, thus stabilizing the liquid foam. The affinity of the IPDA-GO sheets for water is supported by the poly-ionic nature of the functionalized graphene regions. Zeta-potential measurements show

that IPDA-GO is negatively charged in water. Aqueous dispersions of the sheets have a zeta potential of -24 ±1 mV at a pH of 6. This is a lower value than the z-potential of -50 ±1 mV at a pH of 6 observed in aqueous dispersions of GO. The negative zeta-potential observed in IPDA-GO indicates that the surfaces of the shells are negatively charged.

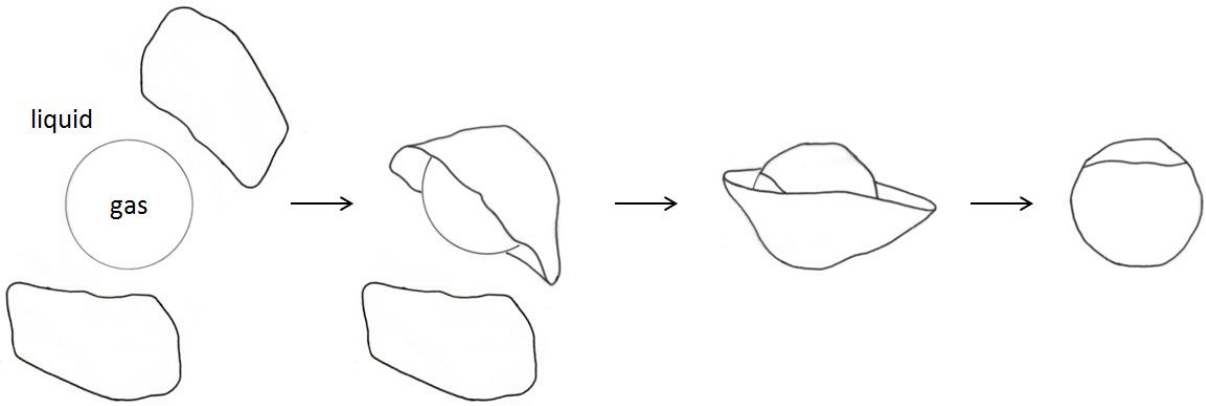

Figure 3-14. Graphene bubble wrapping mechanism.

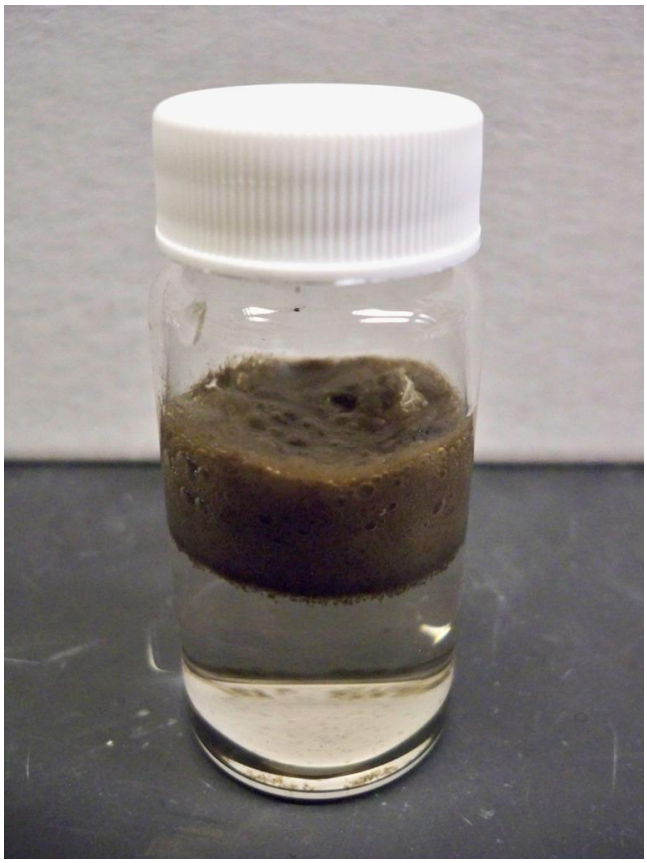

Figure 3-15. LFG 5 hours after its preparation.

The analysis of the LFG shows that the air bubbles are encapsulated inside shells having a concentric layered structure made of IPDA-GO sheets. The IPDA-GO sheets are the foaming agents. The foaming mechanism proposed consists of two steps; the encapsulation of the air bubbles inside the graphene shells and the stabilization of the shelled bubbles in the liquid foam. The encapsulation of the air bubbles is explained on the basis of a wrapping mechanism where the combination of flexibility and barrier properties allows the IPDA-GO sheets to conform to and to content the air bubbles. Hydrophobic forces are suggested to drive the affinity of the sheets towards the gas-liquid interface. Upon encapsulation of the air bubbles, the gas-liquid interface is substituted by a combination of two interfaces, a gas-shell and a shell-liquid interface. The stability of the foams is attributed to the affinity of the functionalized graphene regions in IPDA-GO towards water. In conclusion, the interplay between the hydrophobic graphene regions and the more hydrophilic functionalized graphene regions enables the sheets to, respectively, encapsulate the air bubbles, forming the foam, and avoid a complete phase separation between the shelled bubbles and the liquid, stabilizing the foams.

3.4. Mechanical properties of the graphene shells

The Young's moduli of the graphene shells are estimated from an analysis of their thermal expansion and the pressure inside the bubble just before shell rupture. The pressure inside the bubble is estimated using the ideal gas law as follows

$$PV = nRT$$

$$P_2 = \frac{P_1 V_1 T_2}{T_1 V_2}$$

where P_1 is the atmospheric pressure (0.1 MPa), V_1 is the volume of the bubble at a temperature T_1 (20 °C), P_2 and V_2 are, respectively, the pressure and volume of the bubble at a temperature T_2, n is the number of moles of air in the bubble and R is the ideal gas constant.

Considering that the shell is isotropic in the plane of the sphere, the stress in the shell at a temperature T_2 is estimated from the pressure applied by the air bubble on the internal shell surface over the cross-section area of the shell

$$\sigma = \frac{P_2 r_2}{2t}$$

where r_2 is the radius of the bubble at T_2 and t is the thickness of the shell (5 nm). Shell thickness was estimated by measuring the thickness of freeze-fracture shells as shown in Figure 3-9.

The Young's modulus can then be estimated from Hooke's law in two-dimensions

$$\epsilon_1 = \frac{1}{E}(\sigma_1 - \nu\sigma_2)$$

where ν is the Poisson ratio (assumed to be 1/3), E is the in-plane Young's modulus of the shell, ϵ is the strain due to shell expansion, and $\sigma_1 = \sigma_2$ for equal biaxial tension in the spherical shell. Then

$$E = \frac{\sigma}{\epsilon}(1 - \nu)$$

with

$$\epsilon = \frac{r_2 - r_1}{r_1}$$

The experimental set-up is shown in Figure 3-16. A drop of foam is sandwiched between two glass slides. The bottom slide has been coated with an adhesive and several glass beads deposited to avoid the graphene bubbles from being sandwiched by the glass slides. The volumes of the bubbles are calculated at room temperature, T_1, and at the temperature just before shell rupture, T_2, from the bubble projected area. Volumes are calculated by first measuring the projected area of the bubble, then calculating the radius of the equivalent circle,

and finally using this radius to calculate the volume of the bubble assuming a sphere. This approach is possibly overestimating the radius of the bubble since the shell probably deforms upon contacting the glass slide becoming an ellipsoid. The temperature just before shell rupture, T_2, is the temperature at which the shell fracture line is first detected minus 1 °C. An example of a shell fracture line is shown in Figure 3-17. Results are summarized in Table 3-1.

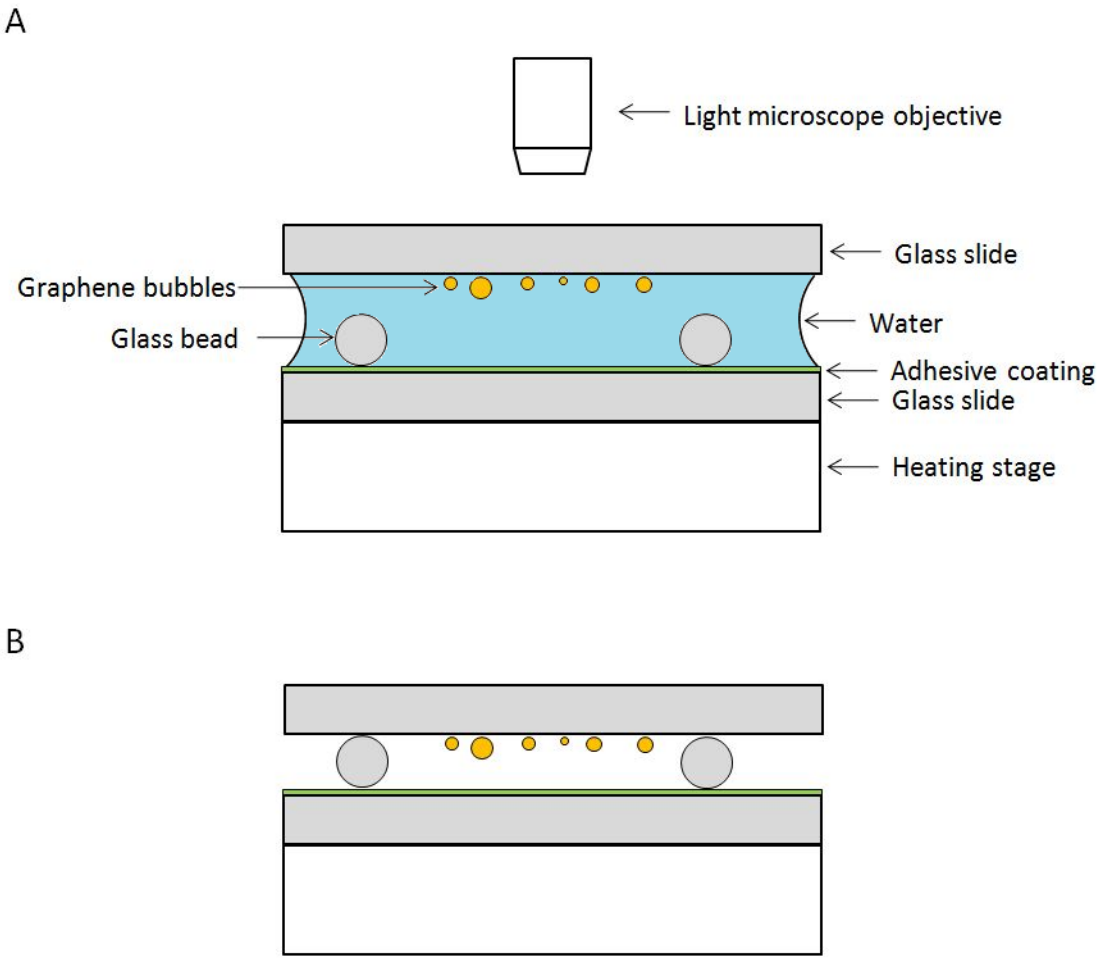

Figure 3-16. Experimental set-up for the thermal expansion study of graphene bubbles. (A) Schematic of the initial configuration of the experiment. (B) Schematic of the experiment after all the water has evaporated. The glass beads prevent the glass slides from applying a force on the graphene bubbles by an eventual sandwiching. The diameter of the glass beads was 245 µm, larger than the diameter of the largest graphene bubble.

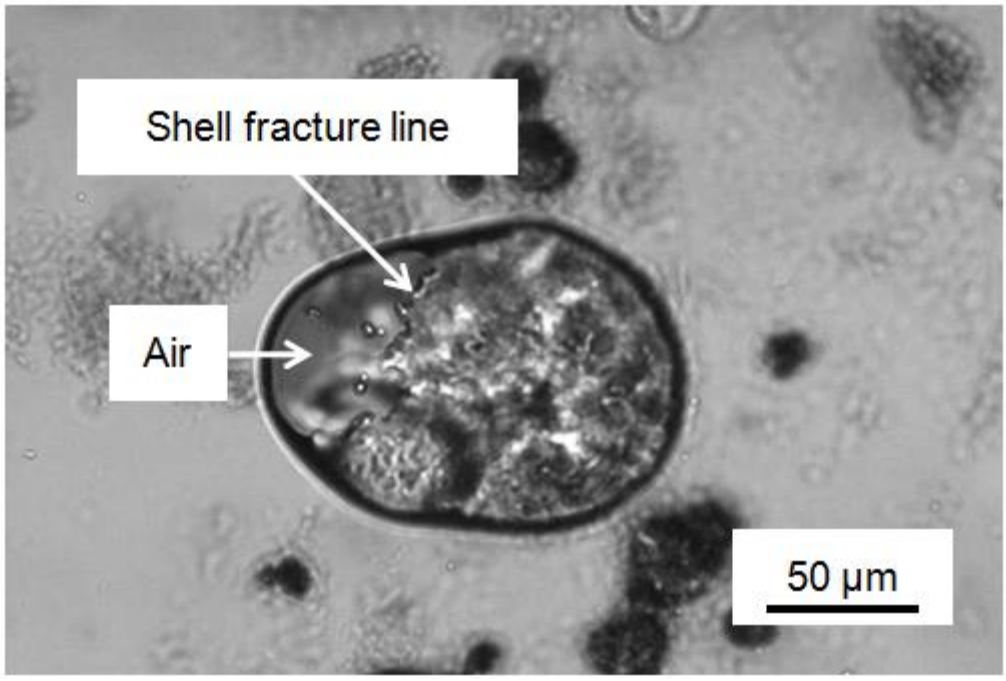

Figure 3-17. Transmission light microscope image of a burst graphene bubble highlighting the shell fracture line and the air bubble coming out of the shell. Sample preparation consisted in sandwiching an aliquot of the foam between glass slides using the set-up shown in Figure 3-16.

The results of this study are summarized in Figure 3-18 and Table 3-1. The Young's moduli of the graphene shells ranged from 1.5 GPa to 2.9 GPa. This range of shell modulus is below the shear modulus in graphite (around 4.5 GPa).[79] Bubbles with diameters below about 30 μm did not burst.

Graphene shells are made of layers of wrinkled IPDA-GO sheets wherein each sheet is different in composition, size and shape. Moreover, shells may present a distribution of thicknesses. All these factors may limit the possibility to observe a clear trend in the shell's mechanical properties. Furthermore, shell deformation and eventual fracture may involve a combination of mechanisms such as the unfolding of the folds, sliding between sheets and tearing of sheets. A deeper understanding of the structural processes at play during the deformation and fracture of the graphene shells would require further investigation.

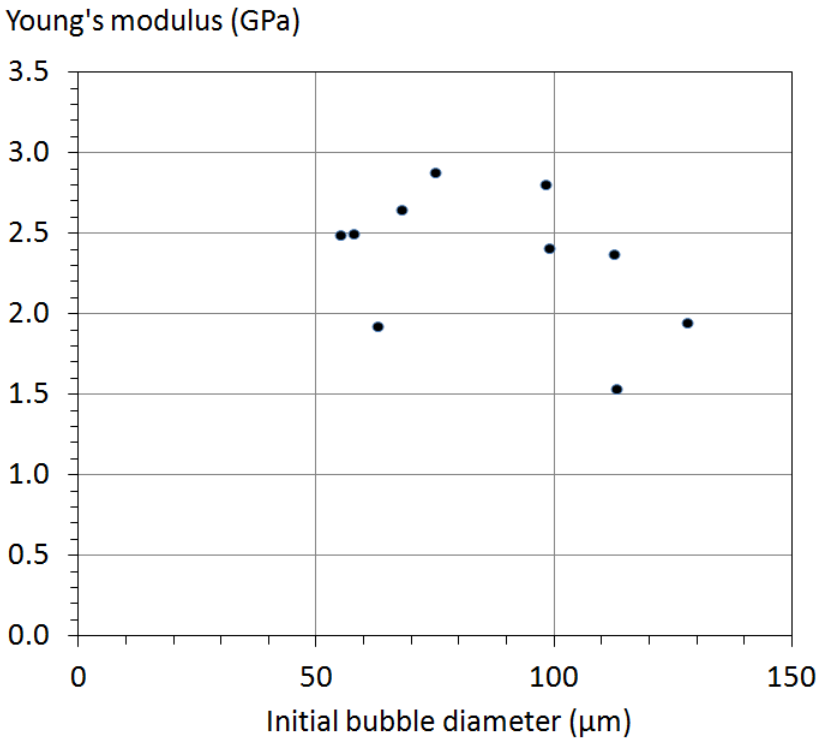

Figure 3-18. Calculated Young's modulus plotted against the initial bubble diameter.

Initial bubble diameter (μm)	Young's modulus (GPa)
75	2.9
128	1.9
113	2.4
98	2.8
99	2.4
113	1.5
55	2.5
63	1.9
68	2.6
58	2.5

Table 3-1. Table summarizing the study on graphene shell mechanical properties.

Chapter 4

Materials and methods

Atomic force microscopy

AFM was conducted on a Nanoscope V with Dimension 3100 (Veeco) using etched single-crystal silicon tips. Measurements were conducted in tapping mode.

Contact angle

Contact angle analysis was conducted on a Rame-Hart apparatus. Pressed films of GO and MGO (foam) were prepared following the XPS sample preparation method reported below. Films were deposited on a silicon substrate via a double sided tape. A series of 2 static contact angle measurements were taken 10 seconds after drop (4 μL of de-ionized water) deposition for the analysis of MGO (foam).

Focused ion beam

FIB milling was conducted on a JEOL 9320 with a 30 kV gallium ion beam. No carbon was deposited prior to milling.

Light microscopy

Light microscopy was conducted on an AxioSkop 2 MAT (Zeiss) and on an Olympus BX41 confocal microscope. Measurements were conducted using polarized and un-polarized white light on the Zeiss.

Scanning electron microscopy

SEM was conducted on a JEOL JSM 6700F. The SEM was operated with an acceleration voltage of 5 kV and in secondary electron imaging mode. Specimens were attached to the SEM sample holder via a double-sided conductive carbon tape.

Thermal expansion of graphene shells

A glass slide was coated with an adhesive layer (Duco Cement, Devcon, ITW Performance Polymers), glass beads of 245 µm in diameter were deposited on the adhesive layer, then a drop of the liquid foam of graphene was deposited on the slide and sandwiched with another glass slide. Figure 3-16 shows a schematic of the experimental set-up. The sample was then deposited on a Linkam heating stage and mounted on the light microscope stage. The heating rate was 5 °C/min.

Transmission electron microscopy

TEM was conducted on a JEOL 2011 operated at 200 kV. Figures 2-14, and 2-16 to 2-18: Sample preparation consisted in casting an aliquot of aqueous dispersions of GO and modified GOs on holey carbon films supported on 200 mesh copper (Cu) grids. Then samples were dried in a dessicator under vacuum of 10 Pa during 24 h. The calibration of the diffraction patterns was conducted with a thin layer of crystalline Au nanoparticles. Au nanoparticles were sputtered on the holey carbon films prior to sample deposition. Figures 3-11 to 3-13: Sample preparation consisted in depositing aliquots of the foam on continuous carbon films supported on 200 mesh copper grids. Then samples were dried in a dessicator under a vacuum of 10 Pa during 24 h.

X-ray diffraction

XRD analysis was conducted on a PANalytical X'Pert Pro operated in Bragg-Brentano geometry and using Cu K_α radiation (λ = 0.154 nm) at 45 kV and 40 mA. Data analysis was conducted with the software package HighScore Plus (PANalytical Inc.). Graphene: As received graphite flakes were deposited on zero background holders. GO and modified forms of GO: Sample preparation followed the same method employed in sample preparation for XPS analysis reported below. The resulting films of GO and modified GOs were deposited on zero background holders. In order to minimize sample contact with ambient moisture, samples were sealed with polyimide films.

X-ray photoelectron spectroscopy

XPS was conducted on an AXIS Ultra DLD Spectrometer (Kratos Analytical) using Al Kα radiation (150 W, x-rays energy 1,486.7 eV) under a base pressure of $7x10^{-7}$ Pa. Data analysis was done using the CasaXPS software package.[80] Graphene: As received graphite flakes were deposited on a copper tape that was attached to the XPS sample holder via a double-sided conductive carbon tape. GO and modified forms of GO: aqueous dispersions of GO and modified forms of GO were dialyzed, freeze-dried and the resulting powders were pressed into films. The films were attached to the XPS sample holder via a double-sided conductive carbon tape.

Zeta potential

Zeta potential analysis was conducted on a PALS Zeta potential analyzer (Brookhaven Instruments). Following an initial calibration with 1mM potassium chloride solution (320 µS

±10%), aqueous dispersions of GO and IPDA-GO where analyzed first to determine particle sizing and then to measure the zeta-potential.

Chapter 5

Conclusions and future directions

This chapter reviews the most important results and outlines future directions for research.

The main outputs of my research have been the invention of the LFG, the initial study of their structure, formation and stability mechanisms, and mechanical properties, and the initial development of the foams into applications. LFG are a new means to manipulate graphene which I think could be of interest from both scientific and technological viewpoints.

There is no account of a physical system that stabilizes air bubbles in a liquid like the LFG. LFG are a new class of liquid foams. IPDA-GO has a sheet molecular structure while surface active foaming agents have chain molecular structures. Figure 4-1 compares both types of liquid foams. A liquid foam made with a foaming agent having a chain molecular structure, exemplified by sodium dodecylsulfate, and the LFG made with IPDA-GO, a foaming agent with a sheet molecular structure.

From a scientific perspective, this thesis has described the basis of the activity of graphene sheets as foaming agents. This is the analysis of the structure of the graphene shells encapsulating the air bubbles and the proposed mechanisms for the formation and stabilization of the foams.

Modifications of graphene other than IPDA-GO could as well result in the formation of liquid foams. I would suggest conducting research aimed at developing chemical modifications of graphene with potential foaming activity.

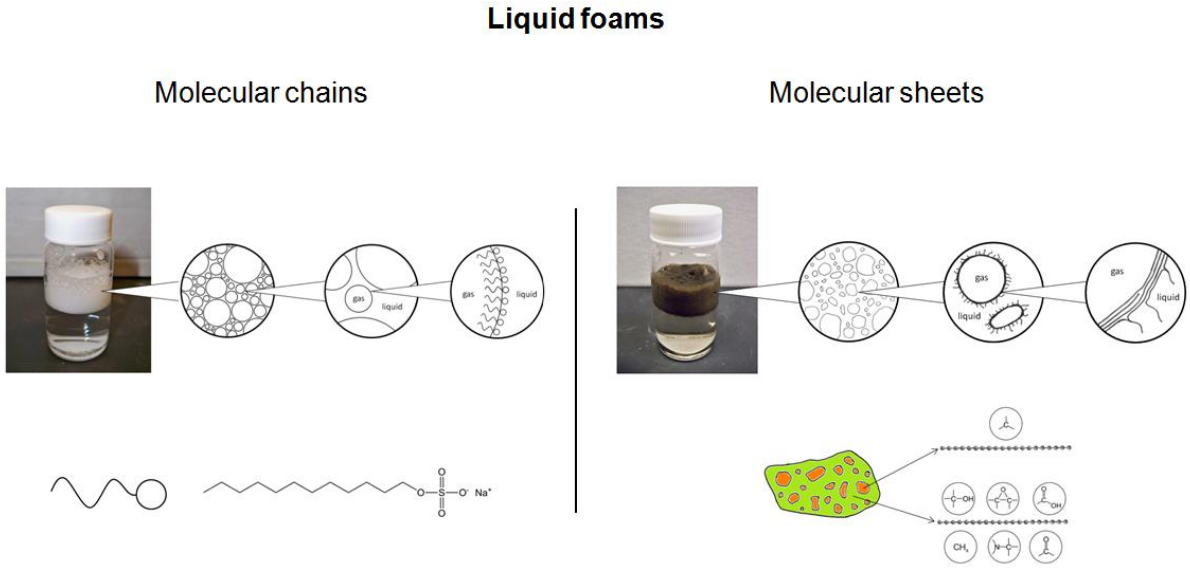

Figure 4-1. Liquid foams made from foaming agents with chain and sheet molecular structures. Hierarchical structures of liquid foams made with (Left) sodium dodecylsulfate and (Right) IPDA-GO.

To gain a better understanding of the graphene foaming mechanism, I would suggest studying those factors that are likely to impact the foam structure such as the size of the graphene sheets and the size of the air bubbles generated during the foaming process. The distribution of bubbles sizes should at least be relevant to the rheology of the foams and hence to processing.

The rheological properties of the LFG should be investigated since they are important to processing but also because of the singularity of the system which could result in unique rheological properties.

Since the size of the bubbles in LFG is the size of the graphene shells, control over the distribution of bubbles sizes should be important in making materials wherein the graphene shells are the building blocks. One example is the preparation of solid cellular graphene foams (CGF) as shown below. Foam aging should be an interesting study.

Although LFG are distinct to traditional surfactant based liquid foams, studies on LFG should take advantage of lessons learned, for example of analytical methods developed, in the study of other liquid foams.

One of the most striking things about the LFG is the thickness of the graphene shells; they are only few nanometers thick yet provide remarkably stable foams. Graphene shells should be an experimental system of interest for fundamental studies of the physical

properties of graphene sheets. Moreover, the robustness of the shells is an advantage when it comes to work the foam.

From a technological perspective, this thesis has explored the use of the LFG as an extractive step in the preparation of graphene-epoxy nanocomposites. It was as part of that effort that the LFG were initially prepared. The foams can be mixed with epoxy pre-polymers resulting in the disassembling of the shells and yielding homogeneous dispersions of sheets in the epoxy matrix. This approach to graphene-epoxy compounding could be extended to polymer systems other than epoxies. Furthermore, the LFG appears to be a powerful means to process graphene beyond the extractive step in the preparation of nanocomposites. The following are two examples of materials prepared from the foams.

Figure 4-2 is a porous network of IPDA-GO sheets prepared after freeze-drying the LFG. Porous structures are of interest in catalysis and in separation processes. This method to fabricate porous networks of graphene sheets respects the chemistry of the sheets since it does not require high temperatures. Hence, such a method has the potential to prepare porous graphene materials with chemically tailored surfaces for the selective detection of specific analytes or scavenging of specific contaminants, for example.

Another type of material that can be made from a LFG is a CGF. Figure 4-3 is a CGF coating made by drying the LFG.[81] Upon drying, the graphene shells pack into a closed-cell foam morphology. There is no liquid in between the shells in a CGF. Considering a shell density ranging from 1 to 3 g/cc (graphite has a density of 2.26 g/cc) the densities of CGF are

estimated at 0.002 to 0.006 g/cc for a shell thickness of 5 nm and diameter of 15 microns. The estimated density of CGF is below the lighter polyimide foams (0.006 g/cc),[82] silica aerogels (0.01-0.3 g/cc),[83] and syntactic carbon foams (0.05-0.25 g/cc).[84] The lower bound estimate would be close to the lower densities reported by Schaedler et al. for metallic micro-trusses (0.001g/cc).[85] Moreover, taking into account the possibility to load the shells with gases together with the encapsulation-release ability of the shells, these cellular systems represent an opportunity to design lightweight functional materials.

LFG should be of interest to a wide variety of scientific and engineering communities looking for new ways to study and apply graphene, as well as to those communities interested in liquid foams in general.

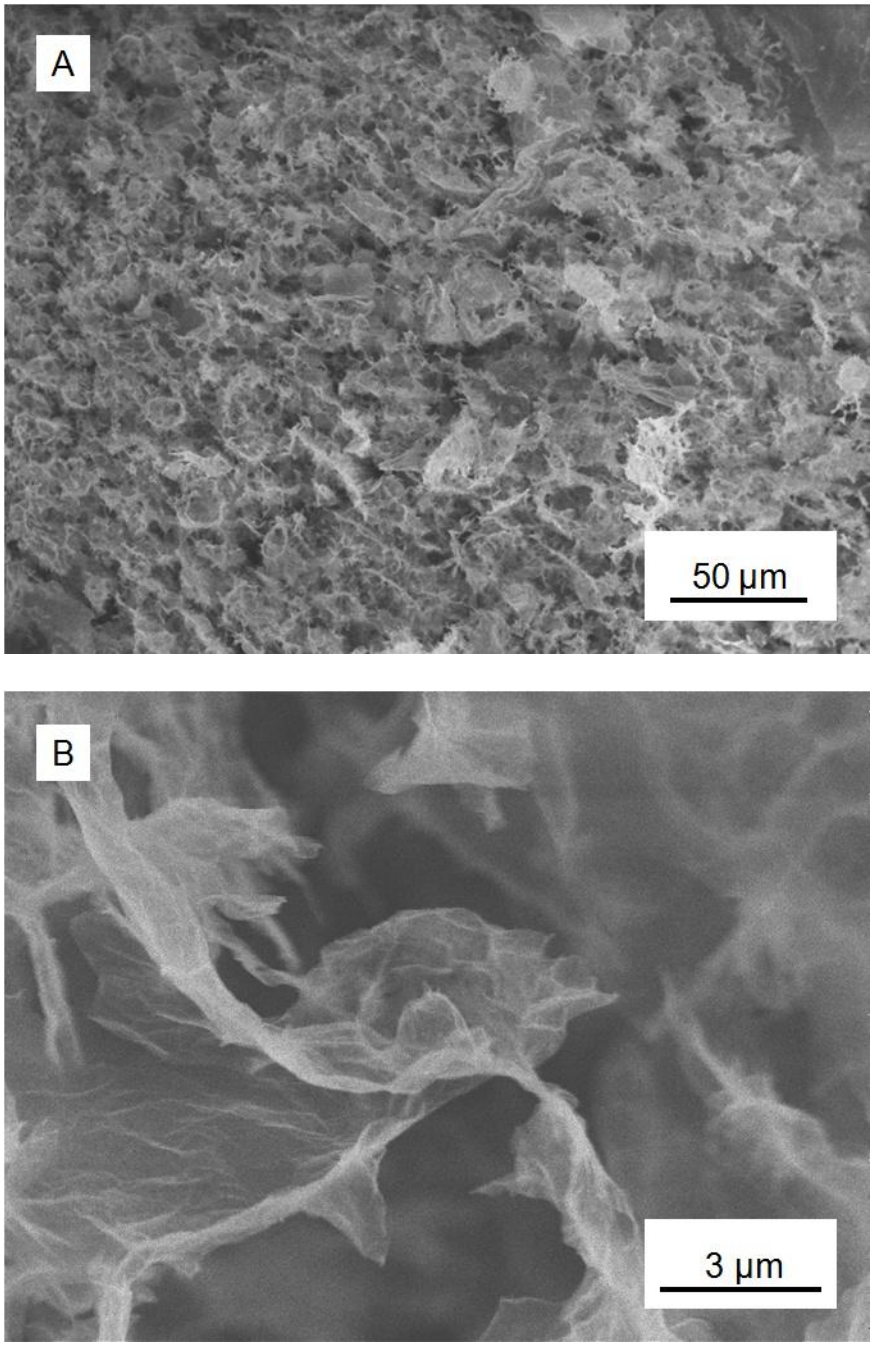

Figure 4-2. SEM imaging of a freeze-dried LFG. (A) Overview of the porosity of the structure, and (B) closer look at the IPDA-GO sheets.

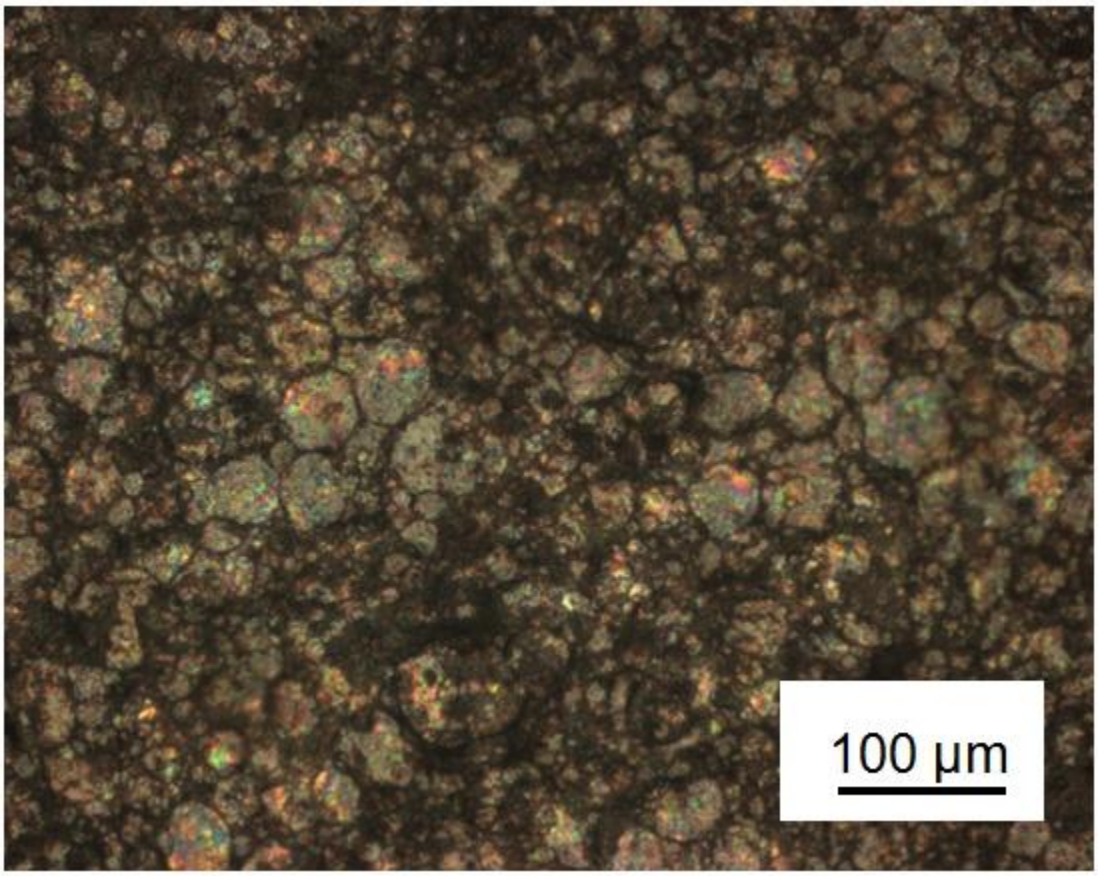

Figure 4-3. Reflexion light microscope image of a cellular graphene coating.

References

1 A. I. Medalia. Nature of carbon black and its morphology in composites. In: Carbon black-polymer composites: the physics of electrically conducting composites. E. K. Sichel (Ed.), Marcel Dekker (1982).

2 W. Hess, C. H. Herd. Microstructure, morphology and general physical properties. In: Carbon black: science and technology. J.-B. Donnet, R. C. Bansal, M.-J. Wang (Eds), Marcel Dekker (1993).

3 G. Kraus. Reinforcement of elastomers by carbon black. Advances in Polymer Science 8, 155 (1971).

4 N. Probst. Conducting carbon black. In: Carbon black: science and technology. J.-B. Donnet, R. C. Bansal, M.-J. Wang (Eds), Marcel Dekker (1993).

5 A. I. Medalia. Nature of carbon black and its morphology in composites. In: Carbon black-polymer composites: the physics of electrically conducting composites. E. K. Sichel (Ed.), Marcel Dekker (1982).

6 L. P. Fox. Rheology of carbon-polymer composites. In: Carbon black-polymer composites: the physics of electrically conducting composites. E. K. Sichel (Ed.) Marcel Dekker (1982).

7 F. H. Gojny, M. H. G. Wichmann, B. Fiedler, K. Schulte. Influence of different carbon nanotubes on the mechanical properties of epoxy matrix composites - A comparative study. Composites Science and Technology 65, 2300 (2005).

8 K. I. Winey, R. A. Vaia. Polymer nanocomposites. MRS Bulletin, 32, 314 (2007).

9 D. Stauffer. Introduction to percolation theory. Taylor & Francis (1992).

10 E. P. Giannelis. Polymer layered silicate nanocomposites. Advanced Materials 8, 29 (1996).

11 A. Usuki, Y. Kojima, M. Kawasumi, A. Okada, Y. Fukushima, T. Kurauchi, O. Kamigaito. Synthesis of nylon 6-clay hybrid. Journal of Materials Research 8, 1179 (1993).

12 P. B. Messersmith, E. P. Giannelis. Synthesis and characterization of layered silicate-epoxy nanocomposites. Chemistry of Materials 6, 1719 (1994).

13 R. A. Vaia, S. Vasudevan, W. Krawiec, L. G. Scanlon, E. P. Giannelis. New polymer electrolyte nanocomposites: melt intercalation of poly(ethy1ene oxide) in mica-type silicates. Advanced Materials 7, 154 (1995).

14 M. Kato, A. Usuki. Polymer-clay nanocomposites. T.J. Pinnavai, G.W. Beall (Eds), John Wiley & Sons (2000).

15 P. B. Messersmith, E. P. Giannelis. Synthesis and barrier properties of poly(epsilon-caprolactone)-layered silicate nanocomposites. Journal of Polymer Science Polymer Chemistry 33, 1047 (1995).

16 S. Iijima. Helical microtubules of graphitic carbon. Nature 354, 56 (1991).

17 Y. L. Li, I. A. Kinloch, A. H. Windle. Direct spinning of carbon nanotube fibers from chemical vapor deposition synthesis. Science 304, 276 (2004).

18 S. B. Sinnott, R. Andrews. Carbon nanotubes: synthesis, properties, and applications. Critical Reviews in Solid State and Materials Sciences 26:3, 145 (2001).

19 M. F. Yu, O. Lourie, M. J. Dyer, K. Moloni, T. F. Kelly, R. S. Ruoff. Strength and breaking mechanism of multiwalled carbon nanotubes under tensile load. Science 287, 637 (2000).

20 M. F. Yu, B. S. Files, S. Arepalli, R. S. Ruoff. Tensile loading of ropes of single wall carbon nanotubes and their mechanical properties. Physical Review Letters 84, 5552 (2000).

21 P. L. McEuen, M. S. Fuhrer, H. Park. Single-walled carbon nanotube electronics. IEEE Transactions on Nanotechnology 1, 78 (2002).

22 A. Bachtold, M. Henny, C. Terrier, C. Strunk, L. Forro. Contacting carbon nanotubes selectively with low-ohmic contacts for four-probe electric measurements. Applied Physics Letters 73, 274 (1998).

23 S. N. Song, X. K. Wang, R. P. H. Chang, J. B. Ketterson. Electronic properties of graphite nanotubules from galvanomagnetic effects. Physical Review Letters 72, 697 (1994).

24 X. Gong, J. Liu, S. Baskaran, R. D. Voise, J. S. Young. Surfactant-assisted processing of carbon nanotube/polymer composites. Chemistry of Materials 12, 1049 (2000).

25 D. Tasis, N. Tagmatarchis, A. Bianco, M. Prato. Chemistry of carbon nanotubes. Chemical Reviews 106, 1105 (2006).

26 F. H. Gojny, M. H. G. Wichmann, B. Fiedler, K. Schulte. Influence of different carbon nanotubes on the mechanical properties of epoxy matrix composites - A comparative study. Composites Science and Technology 65, 2300 (2005).

27 T. H. Hsieh, A. J. Kinloch, A. C. Taylor, I. A. Kinloch. The effect of carbon nanotubes on the fracture toughness and fatigue performance of a thermosetting epoxy polymer. Journal of Materials Science 46, 7525 (2011).

28 J. K. W. Sandler, J. E. Kirk, I. A. Kinloch, M. S. P. Shaffer, A. H. Windle. Ultra-low electrical percolation threshold in carbon-nanotube-epoxy composites. Polymer 44, 5893 (2003).

29 K. S. Novoselov, A. K. Geim, S. V. Morozov, D. Jiang, Y. Zhang, S. V. Dubonos, I. V. Grigorieva, A. A. Firsov. Electric field effect in atomically thin carbon films. Science, 306, 666 (2004).

30 A.W. Moore. Highly oriented pyrolytic graphite. In: Chemistry and physics of carbon Vol. 11. P. L. Walker Jr., P. A. Thrower (Eds), Marcel Dekker (1973).

31 In HOPG, the graphene sheets share a common c-axis orientation, this is the direction normal to the plane of the sheets while in the plane of the sheets there is a statistical distribution of a-axis orientations. The in-plane conductivity (σ_a) in HOPG is $2.5x10^6$ S/m and the c-axis conductivity (σ_c) is $8.3x10^2$ S/m which results in an anisotropy ratio (σ_a / σ_c) of $3x10^3$.

32 M. S. Fuhrer, C. Ning Lau, A. H. MacDonald. Graphene: materially better carbon. MRS Bulletin 35, 289 (2010).

33 J. Scott Bunch, Scott S.Verbridge, Jonathan S. Alden, Arend M. van der Zande, Jeevak M. Parpia, Harold G. Craighead, Paul L. McEuen. Impermeable atomic membranes from graphene sheets. Nano Letters 8, 2458 (2008).

34 M. S. Dresselhaus, G. Dresselhaus. Intercalation compounds of graphite. Advances in Physics 51, 1 (2002).

35 M. S. Fuhrer, C. Ning Lau, A. H. MacDonald. Graphene: materially better carbon. MRS Bulletin 35, 289 (2010).

36 M. Inagaki, F. Kang, M. Toyoda. Exfoliation of graphite via intercalation compounds. In: Chemistry and physics of carbons Vol. 29. L. R. Radovic (Ed.), Marcel Dekker (2004).

37 G. Chen, W. Weng, D. Wu, C. Wu, J. Lu, P. Wang, X. Chen. Preparation and characterization of graphite nanosheets from ultrasonic powdering technique. Carbon 42, 753 (2004).

38 A. Yasmin, J. Luo, I. M. Daniel. Processing of expanded graphite reinforced polymer nanocomposites. Composites Science and Technology 66, 1182 (2006).

39 S.-E. Lee, O. Choi, H. T. Hahn. Microwave properties of graphite nanoplatelet/epoxy composites. Journal of Applied Physics 104, 033705 (2008).

40 L. B. Ebert. Intercalation compounds of graphite. Annual Review of Materials Science 6, 181 (1976).

41 G. R. Hennig. Interstitial compounds of graphite. Progress in inorganic chemistry 1, 125 (1959).

42 N. R. Wilson, P. A. Pandey, R. Beanland, R. J. Young, I. A. Kinloch, L. Gong, Z. Liu, K. Suenaga, J. P. Rourke, S. J. York, J. Sloan. Graphene oxide: structural analysis and application as a highly transparent support for electron microscopy. ACS Nano 3, 2547 (2009).

43 B. C. Brodie. On the atomic weight of graphite. Philosophical Transactions of the Royal Society of London 149, 249 (1859).

44 W. S. Hummers, R. E. Offeman. Preparation of graphitic oxide. Journal of the American Chemical Society 80, 1339 (1958).

45 D. Li, M. B. Muller, S. Gilje, R. B. Kaner, G. G. Wallace. Processable aqueous dispersions of graphene nanosheets. Nature Nanotechnology 3, 101 (2008).

46 G. R. Hennig. Interstitial compounds of graphite. Progress in inorganic chemistry 1, 125 (1959).

47 H. P. Boehm, A. Clauss, G. O. Fischer, U. Hofmann. Das Adsorptionsverhalten sehr dünner Kohlenstoff-Folien. Zeitschrift fuer Anorganische und Allgemeine Chemie 316, 119 (1962).

48 H. P. Boehm , A. Clauss , G. O. Fischer, U. Hofmann. Dünnste Kohlenstoff-Folien. Zeitschrift für Naturforschung B 17 , 150 (1962).

49 S. Stankovich, D. A. Dikin, R. D. Piner, K. A. Kohlhaas, A. Kleinhammes, Y. Jia, Y. Wu, S. T. Nguyen, R. S. Ruoff. Synthesis of graphene-based nanosheets via chemical reduction of exfoliated graphite oxide. Carbon 45, 1558 (2007).

50 S. Stankovich, D. A. Dikin, G. H. B. Dommett, K. M. Kohlhaas, E. J. Zimney, E. A. Stach, R. D. Piner, S. T. Nguyen, R. S. Ruoff. Graphene-based composite materials. Nature 442, 282 (2006).

51 B. C. Brodie. On the atomic weight of graphite. Philosophical Transactions of the Royal Society of London 149, 249 (1859).

52 R. C. Croft. Lamellar compounds of graphite. Quarterly Reviews, Chemical Society,

14, 1 (1960).

53 H. C. Schniepp, J. L. Li, M. J. McAllister, H. Sai, M. Herrera-Alonso, D. H. Adamson, R. K. Prud'homme, R. Car, D. A. Saville, I. A. Aksay. Functionalized single graphene sheets derived from splitting graphite oxide. The Journal of Physical Chemistry B 110, 8535 (2006).

54 (a) S. Park, R. S. Ruoff, Chemical methods for the production of graphenes. Nature Nanotechnology 4, 217 (2009).

(b) J. I. Paredes, S. Villar-Rodil, M. J. Fernandez-Merino, L. Guardia, A. Martinez-Alonso, J. M. D. Tascon. Environmentally friendly approaches toward the mass production of processable graphene from graphite oxide. Journal of Materials Chemistry 21, 298 (2011).

(c) T. Kuilla, S. Bhadrab, D. Yaoa, N. H. Kim, S. Bosed, J. H. Lee. Recent advances in graphene based polymer composites. Progress in Polymer Science 35, 1350 (2010).

(d) J. R. Potts, D. R. Dreyer, C. W. Bielawski, R. S. Ruoff. Graphene-based polymer nanocomposites. Polymer, 52, 5 (2011).

(e) H. Kim, A. A. Abdala, C. W. Macosko. Graphene/polymer nanocomposites. Macromolecules 43, 6515 (2010).

55 W. S. Hummers, R. E. Offeman. Preparation of graphitic oxide. Journal of the American Chemical Society 80, 1339 (1958).

56 K. S. Novoselov, A. K. Geim, S. V. Morozov, D. Jiang, Y. Zhang, S. V. Dubonos, I.

V. Grigorieva, A. A. Firsov. Electric field effect in atomically thin carbon films. Science 306, 666 (2004).

57 H. Estrade-Szwarckopf, B. Rousseau. U.P.S. and X.P.S. Studies of alkali-graphite intercalation compounds. Synthetic Metals, 23, 191 (1988).

58 M. P. Seah. Charge referencing techniques for insulators. In: Practical surface analysis by auger and x-ray photoelectron spectroscopy. D. Briggs, M. P. Seah (Eds), John Wiley and Sons (1983).

59 H. Estrade-Szwarckopf. XPS photoemission in carbonaceous materials: A ‘‘defect’’ peak beside the graphitic asymmetric peak. Carbon 42, 1713 (2004).

60 D. Briggs. Applications of XPS in Polymer Technology. In: Practical surface analysis by auger and x-ray photoelectron spectroscopy. D. Briggs, M. P. Seah (Eds), John Wiley and Sons (1983).

61 High resolution XPS of organic polymers: the Scienta ESCA300 database. G. Beamson, D. Briggs (Eds). John Wiley and Sons (1992).

62 P. M. Th. M. van Attekum, G. K. Wertheim. Excitonic effects in core-hole screening. Physical Review Letters 43, 1896 (1979).

63 F. Sette, G. K. Wertheim, Y. Ma, G. Meigs, S. Modesti, C. T. Chen. Lifetime and screening of the C 1s photoemission in graphite. Physical Review Letters B 41, 9766 (1990).

64 S. Doniach, M. Sunjic. Many-electron singularity in x-ray photoemission and x-ray line spectra from metals. Journal of Physics C: Solid State Physics 3, 285 (1970).

65 H. Estrade-Szwarckopf. XPS photoemission in carbonaceous materials: A ‘‘defect’’

peak beside the graphitic asymmetric peak. Carbon 42, 1713 (2004).

66 J. Y. Howe, C. J. Rawn, L. E. Jones, H. Ow. Improved crystallographic data for graphite. Powder Diffraction 18, 150 (2003).

67 R. E. Franklin. The structure of graphitic carbons. Acta Crystallographica 4, 253 (1951).

68 H. P. Klug, L. E. Alexander. X-ray Diffraction procedures for polycrystalline and amorphous materials. John Wiley & Sons (1974).

69 A. Buchsteiner, A. Lerf, J. Pieper. Water dynamics in graphite oxide investigated with neutron scattering. The Journal of Physical Chemistry B 110, 22328 (2006).

70 N. R. Wilson, P. A. Pandey, R. Beanland, R. J. Young, I. A. Kinloch, L. Gong, Z. Liu, K. Suenaga, J. P. Rourke, S. J. York, J. Sloan. Graphene oxide: structural analysis and application as a highly transparent support for electron microscopy. ACS Nano 3, 2547 (2009).

71 W. P. Davey. Precision measurements of the lattice constants of twelve common metals. Physical Review 25, 753, (1925).

72 J. C. Meyer, A. K. Geim, M. I. Katsnelson, K. S. Novoselov, T. J. Booth, S. Roth. The structure of suspended graphene sheets. Nature 446, 60 (2007).

73 A. Saint-Jalmes, D. J. Durian, D. A. Weitz. Foams. In: Kirk-Othmer encyclopedia of chemical technology (2004).

74 D. Weaire, S. Hutzler. The physics of foams. Oxford University Press (1999).

75 D. Myers. Surfactant science and technology. Wiley-Interscience (2006).

76 T. Tadros. Surfactants. In: Kirk-Othmer encyclopedia of chemical technology

(2006).

77 T. A. Witten. Stress focusing in elastic sheets. Reviews of Modern Physics 79, 643 (2007).

78 K. H. Storks. An electron diffraction examination of some linear high polymers. Journal of the American Chemical Society 60, 1753 (1938).

79 H. O. Pierson. Handbook of carbon, graphite, diamond and fullerenes. Noyes Publications (1993).

80 N. Fairley. CasaXPS Manual 2.3.15 Spectroscopy. Casa Software Ltd. (2009).

81 L. J. Gibson, M. F. Ashby. Cellular solids: structure and properties. Cambridge University Press (1997).

82 Evonik Degussa Solimide.

83 MarkeTech International.

84 C. R. Thomas. Syntactic carbon foams. Materials Science and Engineering, 12, 219 (1973).

85 T. A. Schaedler, A. J. Jacobsen, A. Torrents, A. E. Sorensen, J. Lian, J. R. Greer, L. Valdevit, W. B. Carter. Ultralight metallic microlattices. Science, 334, 962 (2011).